nature

ARTICLES

Probabilistic assessment of sea level during the last interglacial stage

Robert E. Kopp[1,2], Frederik J. Simons[1], Jerry X. Mitrovica[3], Adam C. Maloof[1] & Michael Oppenheimer[1,2]

With polar temperatures ~3–5 °C warmer than today, the last interglacial stage (~125 kyr ago) serves as a partial analogue for 1–2 °C global warming scenarios. Geological records from several sites indicate that local sea levels during the last interglacial were higher than today, but because local sea levels differ from global sea level, accurately reconstructing past global sea level requires an integrated analysis of globally distributed data sets. Here we present an extensive compilation of local sea level indicators and a statistical approach for estimating global sea level, local sea levels, ice sheet volumes and their associated uncertainties. We find a 95% probability that global sea level peaked at least 6.6 m higher than today during the last interglacial; it is likely (67% probability) to have exceeded 8.0 m but is unlikely (33% probability) to have exceeded 9.4 m. When global sea level was close to its current level (≥−10 m), the millennial average rate of global sea level rise is very likely to have exceeded 5.6 m kyr^{-1} but is unlikely to have exceeded 9.2 m kyr^{-1}. Our analysis extends previous last interglacial sea level studies by integrating literature observations within a probabilistic framework that accounts for the physics of sea level change. The results highlight the long-term vulnerability of ice sheets to even relatively low levels of sustained global warming.

As a result of industrial activity, greenhouse gas concentrations now exceed levels reached on Earth at any time within the past 800 kyr (ref. 1). Given a climate sensitivity of 2–4.5 °C per doubling of carbon dioxide levels[2], current greenhouse gas concentrations—without considering any further increases—are sufficient to cause an equilibrium warming of 1.4–3.2 °C. Among the many effects expected to accompany this warming is a rise in global sea level (GSL)[2], which is defined as the mean value of local sea level (LSL) taken across the ocean. This rise is driven primarily by thermal expansion of sea water and by melting land ice. Uncertainties in ice sheet behaviour make it difficult to predict sea level rise using prognostic models, but by the end of the twenty-first century, GSL could exceed today's value by more than one metre (refs 3, 4). As changes of this magnitude have no precedent in recorded history, to understand them and to compile observations against which to test models of future climate change, it is necessary to turn to the geological record.

In this Article, we analyse a new compilation of geographically dispersed sea level indicators spanning the last interglacial stage (LIG), which climaxed about 125,000 years ago (125 kyr ago). The LIG (also known as the Eemian stage, its local northern European name, and as Marine Isotope Stage 5e) is of special interest for three reasons: (1) it is recent enough that it is possible to obtain some sea level records with high temporal resolution and many more observations with lower temporal resolution; (2) due in large part to enhanced Northern Hemisphere insolation, global and polar temperatures may have been slightly warmer than at present; and (3) several lines of evidence suggest that GSL was higher than today, perhaps by 4–6 m (ref. 1), and that the Greenland Ice Sheet and possibly also the West Antarctic Ice Sheet[5,31] were significantly smaller than they are now.

During the LIG, greenhouse gas concentrations were comparable to pre-industrial Holocene levels[7], but Earth's orbital eccentricity was more than twice the modern value[8]. Energy balance modelling predicts that, as a consequence, summer temperatures between 132 and

124 kyr ago on all land masses except Antarctica were at least 0.5 °C warmer than today[9], while a more complete climate model indicates summer temperatures 2–4 °C warmer than today in most of the Arctic[6]. Ice core data from both Greenland and Antarctica suggest polar temperatures in both hemispheres of about 3–5 °C warmer than today[1], comparable to the 3–6 °C of Arctic warming that is expected to accompany 1–2 °C of global warming[10]. In Europe, pollen data suggest middle Eemian summer temperatures about 2 °C warmer than present[11]. While the change in global mean temperature is uncertain, sea surface temperatures in the equatorial Pacific[12] and Atlantic[13] were about 2 °C warmer than pre-industrial levels.

Synthesizing geological sea level indicators into a global reconstruction requires accounting for regional variability. Differences between LSL and GSL arise because—contrary to an analogy commonly taught in introductory classes—adding water from melting land ice to the ocean is not like pouring water into a bathtub. Many factors other than the changing volume of water in the ocean modulate the influence of melting ice sheets on LSL. These factors include: the direct gravitational effect of the distribution of ice, water and sediment on the sea surface (or geoid), solid Earth deformation and its associated gravitational signature, perturbations to both the magnitude and orientation of the Earth's rotation vector, and time-varying shoreline geometry[14–16], as well as changes in ocean and atmosphere dynamics[17]. In addition, LSLs are influenced by tectonic uplift and thermal subsidence.

As a consequence of these factors, LSLs at Pacific islands far from the late Pleistocene ice sheets were 1–3 m higher in the middle Holocene than today, even though GSL was essentially unchanged[18]. Similarly, even if GSL was never higher than today, LSLs several metres higher than present could have occurred far from the former Laurentide Ice Sheet (for example, in Australia) early in the LIG, and comparably high LSLs could have occurred closer to the former ice sheet (for example, in the Caribbean) late in the LIG[19]. Without accurate and precise dating of the relevant sea level indicators and an appreciation of the difference between LSL and GSL, such patterns could

[1]Department of Geosciences, [2]Woodrow Wilson School of Public and International Affairs, Princeton University, Princeton, New Jersey 08544, USA. [3]Department of Earth and Planetary Sciences, Harvard University, Cambridge, Massachusetts 02138, USA.
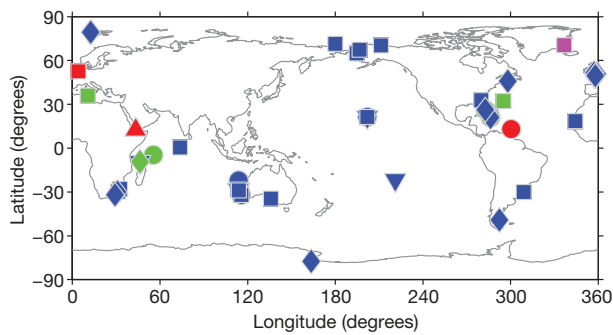
Figure 1 | Sites with at least one sea level observation in our database. The symbol shapes reflect the nature of the indicators (upward triangles, isotopic; circles, reef terraces; downward triangles, coral biofacies; squares, sedimentary facies and non-coral biofacies; diamonds, erosional). The colours reflect the number of observations at a site (blue, 1; green, 2; magenta, 3; red, 4 or more).

produce the false appearance of a magnified or diminished GSL highstand. In order to estimate ice sheet history from sea level records, it is thus necessary to account for physical factors like gravitation and solid Earth deformation. Conversely, because these effects cause LSL changes to differ with distance from an ice sheet, a global database of LSL indicators can potentially address not just whether global ice volume was smaller during the LIG than today, but also what combination of melting ice sheets, if any, was responsible for higher GSL.

We construct a database of sea level indicators that is as comprehensive as possible (Figs 1, 2; full data set available in Supplementary Information) and use it to estimate the posterior probability distribution of LSL as a function of space and time and of GSL and ice sheet volumes as functions of time. We must cope with variable geochronological uncertainty, as well as with variable errors in sea levels

inferred from proxy data and in estimates of regional long-term tectonic uplift or thermal subsidence. In addition, some of the data provide only upper or lower bounds to sea level. Where possible, we also want to take advantage of quasi-continuous sequences, in which relative timing is known with greater precision than absolute dates. These sequences include a stacked global oxygen isotope curve from benthic foraminifera[20], as well as series of LSL measurements inferred from sedimentary facies in the Netherlands[21] and from hydrological modelling of foraminiferal oxygen isotopes in the Red Sea[22]. (These series are described in detail in Supplementary Information.)

Statistical approach

The ultimate goal of our analysis is to determine the posterior probability distribution of LIG sea level and ice volume through time, conditioned upon the measurements in our database. Inherent in the method is the assumption that both the prior and posterior distributions are multivariate Gaussian.

We construct a prior probability distribution from the global oxygen isotope curve and its associated age model[20], as described in detail in Methods and Supplementary Information. To do this, we use a physical model of LSL that calculates the eustatic, gravitational, deformational and rotational effects of melting ice sheets[15,16,23]. We estimate the mean and covariance of the prior distribution by averaging the values and covariances of the LSLs and of GSL obtained by running many alternative ice sheet histories through a forward physical model. These histories themselves are sampled from two underlying distributions: a distribution for global ice volume over time based upon ref. 20 and a distribution for individual ice sheet volumes conditioned upon global ice volume. This latter distribution is based upon random perturbations of a model of Last Glacial Maximum (LGM)-to-present ice sheet volume[24] with additional allowances made for ice sheets smaller than their present volumes. To approximate thermosteric effects resulting
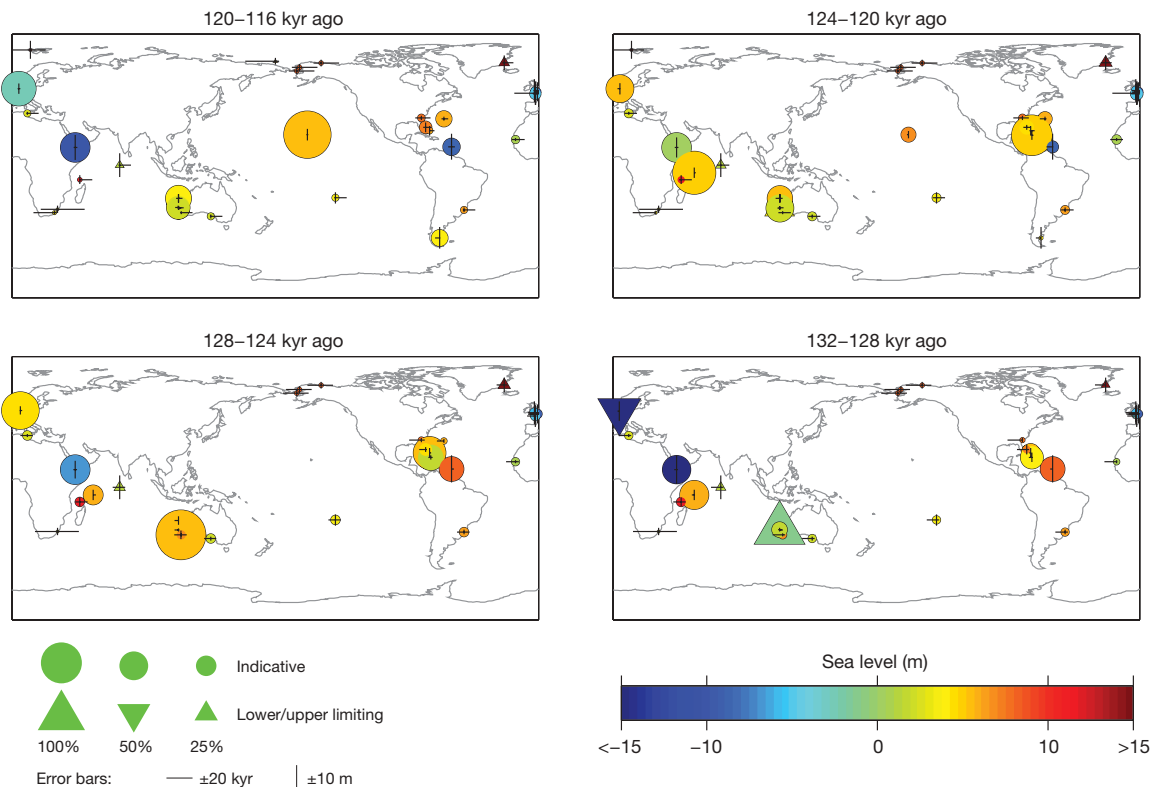

Figure 2 | Localities at which LSL data exist in our database, for time slices through the LIG. The diameter of each circle scales as indicated with the probability that the corresponding data point occurs in the indicated interval. The horizontal (vertical) lines are proportional to the standard deviations of the age (sea level) measurements. The intersection of the lines reflects the mean age estimate relative to the age window; a rightward skew

reflects a mean estimate earlier than the middle of the window. Data that provide only upper or lower sea level bounds are indicated by downward and upward triangles, respectively. Colours indicate the mean sea level estimate in metres above present value. Some symbols overlap; for a complete table of observations, see Supplementary Information.

from changes in mean ocean temperature and salinity, we add two Gaussian terms: a term independent of time and GSL with a mean of 0 m and a standard deviation of 2 m, and a term that varies with global ice volume (-1.6 ± 0.6 m per 100 m equivalent sea level (e.s.l.) ice sheet growth). The temporal covariance of these thermosteric terms has an e-folding time of 2 kyr. The uncertainty within the thermosteric terms is large enough to also accommodate small contributions from other sources, such as small mountain glaciers present today but not included in the LGM-to-present ice model.

To construct the posterior distribution of sea level at any arbitrary point in space and time, we start with the simpler problem of estimating the posterior probability distribution of sea level at the points included in our database and then interpolate to calculate values at points not in our database. We employ a three-step Gibbs sampler[25] to sample the Bayesian network illustrated in Fig. 3.

In the first step, we calculate corrected measurements of LSLs (**s**) by adjusting the altitude of our proxy observations (**z**) for their depositional settings (**D**), which account for the relationship between proxy altitudes and sea level elevation at the time of formation, and for the background regional uplift or subsidence. The former correction incorporates sedimentological and geomorphological knowledge, such as the fact that most coral observations in the database are of species that grow between 0 and 5 m below mean low tide level[26,27], as well as information about local tidal range. The latter correction is based upon an estimate of the regional uplift or subsidence rate (**u**) and a sample from the posterior distribution of measurement ages (**g**). In selecting or constructing uplift or subsidence rate estimates, we have avoided estimates from the literature that assume LIG sea level as a reference point.

In the second step, we employ Gaussian process regression to estimate the true sea levels (**f**). Gaussian process regression[28], of which the commonly used geospatial technique of kriging interpolation is a well-known example, treats a field (such as sea level) as a collection of random variables drawn from a multivariate Gaussian distribution. By specifying the covariance structure of the field, knowledge about the relevant physics affecting the process can be incorporated into the modelling without constraining it to fit a particular forward model.

In the third step, we use the Metropolis-Hastings algorithm[29] to draw a new Markov chain Monte Carlo sample of the ages (**g**), based upon the measured ages (**t**) and the current estimate of the true sea
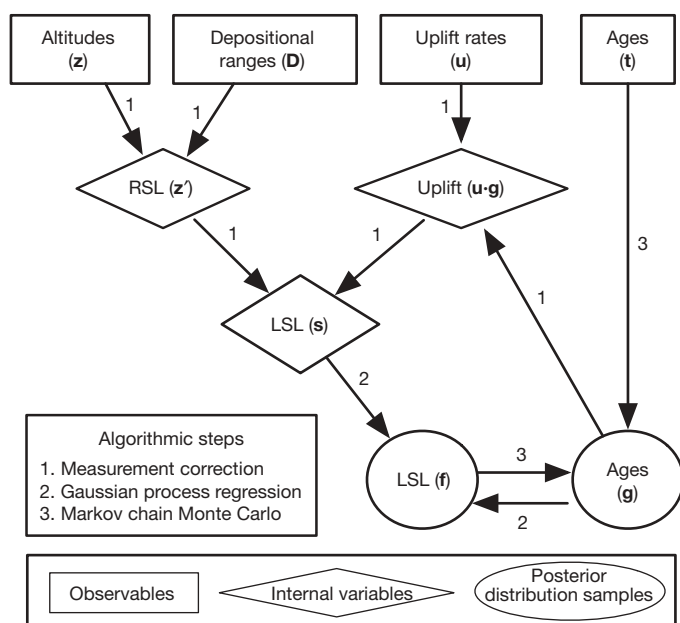
levels (**f**). Repeating this sequence many times allows us to sample the posterior probability distribution for LSL and GSL in a way that satisfies the measurements to within their uncertainties.

Equipped with an estimate of the posterior probability distribution, we can then answer questions such as 'what was the maximum GSL attained during the LIG' and 'what was the fastest rate at which GSL rose when it was within 10 m of its present value?' (As discussed below, we focus on rates above the -10 m threshold because the Laurentide Ice Sheet was comparable in size to the modern Greenland Ice Sheet by the time GSL rose to this level in the Holocene.) To answer such questions, we draw many samples from the posterior distribution and examine the distribution of answers based on these samples. We report these answers as exceedance values. For instance, the 95% probability exceedance value of GSL is exceeded in 95% of all samples. If the 95% exceedance value is 6.6 m, we can reject the hypothesis that sea level never exceeded 6.6 m at the 95% confidence level. Note that the answer to such questions is not identical to the answer one would get by looking at the median projection of GSL and reading its maximum; the maximum of the median would be the 50% probability exceedance value if all time points were perfectly correlated, but such is not the case. The median reconstruction instead represents the best estimate for GSL at each specific point in time, whereas the exceedance values are calculated across the entire LIG interval.

Results of global analysis

Applying our algorithm to the full data set of LIG sea level indicators yields a GSL curve (Fig. 4a) with a median projection that peaks at 124 kyr ago at 7.2 ± 1.3 m (67% confidence interval). Further analysis reveals a 95% probability of having exceeded 6.6 m at some time during the LIG highstand and a 67% probability of having exceeded 8.0 m (Fig. 5, solid line). It is unlikely (33% probability) that GSL exceeded 9.4 m.

To test the sensitivity of these results, we analysed seven subsets of the data: one subset excluding the Red Sea oxygen isotope curve, and six either excluding or including only (1) coral data, (2) erosional features, or (3) facies interpretations (Supplementary Information).
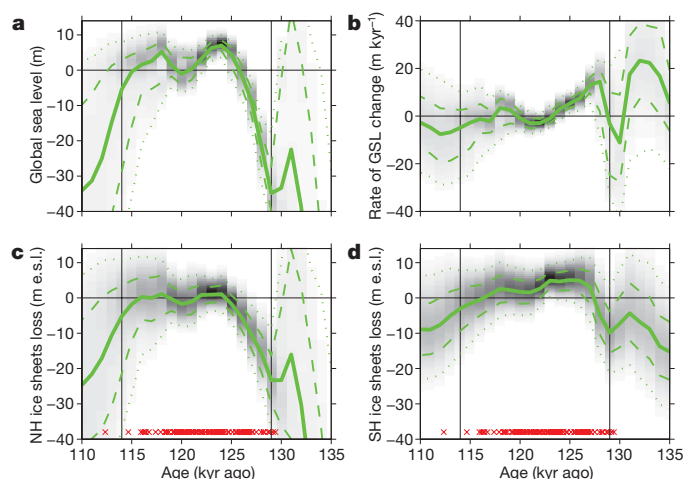

Figure 3 | Schematic illustration of the process used in our statistical analysis. See text for details.

Figure 4 | Probability density plots of GSL and ice volume during the LIG.
a, Global sea level (GSL); **b**, 1,000-year average GSL rates; **c**, Northern Hemisphere (NH) ice volume; and **d**, Southern Hemisphere (SH) ice volume. Heavy lines mark median projections, dashed lines the 16th and 84th percentiles, and dotted lines the 2.5th and 97.5th percentiles. Red crosses mark median posterior estimates of sample ages. Vertical lines mark the interval when >30% of samples from the distribution have standard deviations of GSL <30% of the prior standard deviation (and are thus included in calculations of exceedance probabilities). The horizontal line at 0 indicates modern values in **a**, **c** and **d** and unchanging GSL in **b**. We urge caution in interpreting ice volume projections (**c**, **d**) owing to the use of a Gaussian distribution to represent a non-Gaussian prior. e.s.l., equivalent sea level.
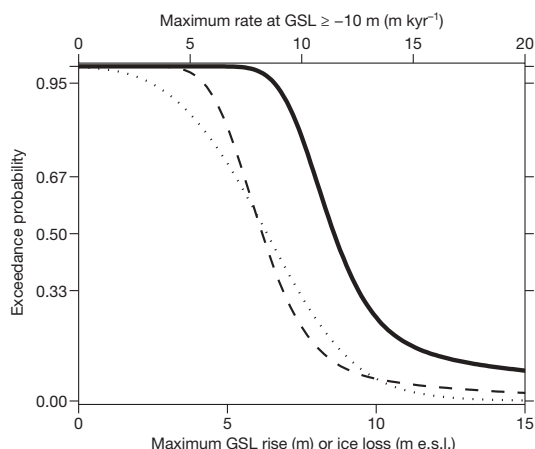
Figure 5 | Exceedance values calculated from the posterior probability distribution. The solid line shows GSL rise, the dashed line shows the 1,000-year average rate of change of GSL when GSL is at or above −10 m, and the dotted line shows ice loss in the hemisphere with the least ice loss.

The results from these subsets were fairly consistent. Across all subsets, the median projection peaked between 6.4 and 8.7 m. With the exception of the subset containing only erosional features, the 95% probability exceedance value ranged from 5.7 to 7.0 m, the 67% probability value ranged from 7.3 to 8.7 m, and the 33% probability value ranged from 8.4 to 10.5 m. (The values for the subset containing only erosional features were slightly lower and more broadly spread, with 95%, 67% and 33% values of −0.3 m, 3.9 m and 6.8 m, respectively. The spread reflects the relatively high uncertainty on this projection, which results in large part from a smaller data set.) We therefore consider our results to be reasonably robust with respect to different observations.

The 95%, 67% and 33% probability exceedance values for 1,000-year average GSL rise rate during the interval when GSL was ≥ -10 m are 5.6 m kyr^{-1}, 7.4 m kyr^{-1} and 9.2 m kyr^{-1}, respectively (Fig. 4b; Fig. 5, dashed line). We emphasize that these values by no means exclude faster intervals of sea level rise lasting for less than one millennium.

We can also attempt to answer questions about the magnitude of ice sheet volume based on the posterior probability distribution, but we must do so with caution. The distribution of Northern Hemisphere ice volume, in particular, can only be roughly approximated with a Gaussian, as it has a hard upper bound set by the fact that there is only about 7 m e.s.l. of Northern Hemisphere ice available to melt today. Because of this limitation, although we directly present the hemispheric ice volume posteriors in Fig. 4c, d, we make only one fairly conservative inference regarding ice sheet volumes. The posterior distribution suggests a 95% probability that both Northern Hemisphere ice sheets and Southern Hemisphere ice sheets reached minima at which they were at least 2.5 m e.s.l. smaller than today, although not necessarily at the same point in time (Fig. 5, dotted line). We can make no strong statements about in which hemisphere the ice shrunk to a greater extent; in 59% of samples, it was the Southern Hemisphere and in 41% of samples, it was the Northern Hemisphere. Additional sea level proxies close to the ice sheets would help increase the precision of these estimates, as might a non-Gaussian model for the prior distribution.

Comparison to previous estimates

Previous estimates of LIG sea level, which were generally in the range 4–6 m, were based on interpretations of LSL at a small number of localities. The Fourth Assessment Report of the IPCC[1] highlighted Hawaii and Bermuda[30]; other authors[31] also include observations from the Bahamas, Western Australia and the Seychelles Islands. All these localities are relatively tectonically stable and experience only slow thermal subsidence, associated with the cooling of the lithosphere. If one had to draw conclusions about GSL from a small

number of LSL measurements, these are reasonable sites at which to look.

Other commonly considered localities, such as Barbados[32] and the Huon Peninsula[33], are rapidly uplifting localities. These sites have advantages as relative sea level recorders, most notably that terraces recording sea levels below present are readily accessible. Assuming these sites have experienced a steady rate of uplift, they can help uncover sea level variations over fairly short timescales. However, they are poor sites from which to draw conclusions about absolute sea levels, as recovering this information requires a precise estimate of uplift rate. Because our method incorporates knowledge about the associated uncertainties, we can include both stable and uplifting sites into our analysis.

To our knowledge, only one previous study[19], which used a fairly limited set of observations, has attempted to account for the effects of glacial isostatic adjustment in drawing conclusions about GSL and ice volume from LIG sea level records. As that study demonstrated, understanding the influence of these effects is critical, as otherwise LSL highstands could easily be falsely interpreted as reflecting global highstands. Our statistical model uses the covariance between local and GSL, derived from many runs of a forward physical model, to account for the gravitational, deformational and rotational effects of the ice–ocean mass redistribution. Our results indicate that the apparent high GSL during the LIG is indeed real, though previously underestimated.

Rates of sea level change

Our results suggest that during the interval of the LIG when sea level was above −10 m, the rate of sea level rise, averaged over 1 kyr, was very likely to have reached values of at least about 5.6 m kyr^{-1} but was unlikely to have exceeded 9.2 m kyr^{-1}. Our data do not permit us to resolve confidently rates of sea level change over shorter periods of time. Our inferences are consistent with estimates of the rate of the contribution of Laurentide Ice Sheet meltwater to GSL during the early Holocene; the Laurentide Ice Sheet contribution is estimated to account for about 7 m kyr^{-1} during the period when GSL climbed above −10 m (ref. 34).

Ice volume during the late deglacial rise at the start of the LIG was only slightly larger than at present. The Laurentide Ice Sheet would have been a shrunken remnant of its once extensive mass—or, perhaps two small remnants, one over Québec and Labrador and one over eastern Nunavut and Baffin Island, as in the early Holocene[34,35]. As the Laurentide Ice Sheet was within a factor of two in size of the present Greenland Ice Sheet, its dynamics may have been analogous to those of the Greenland Ice Sheet. The results from the LIG suggest that, given a sufficient forcing, the present ice sheets could sustain a rate of GSL rise of about 56–92 cm per century for several centuries, with these rates potentially spiking to higher values for shorter periods.

Discussion

Although it is the approach most commonly taken when the LIG is used as an analogue for near-future warming, GSL and global ice volume cannot be accurately inferred by a qualitative examination of LSL at a handful of localities. Better control is afforded by a more thorough approach that combines, as we do, an extensive database of sea level indicators with a probabilistic assessment of their interpretive and geochronological errors. The results of our analysis support the common hypothesis that LIG GSL was above the current value, but contrary to previous estimates, we conclude that peak GSL was very likely to have exceeded 6.6 m and was likely to have been above 8.0 m, though it is unlikely to have exceeded 9.4 m.

The LIG was only slightly warmer than present, with polar temperatures similar to those expected under a low-end, ~2 °C warming scenario. Nonetheless, it appears to have been associated with substantially smaller ice sheets than exist at present. Achieving GSL in excess of 6.6 m higher than present is likely to have required major melting of both the Greenland and the West Antarctic ice sheets, an

inference supported by our finding that both Northern and Southern hemisphere ice volumes are very likely to have shrunk by at least 2.5 m e.s.l. relative to today. Incorporating a large database of palaeo-climatic constraints thus highlights the vulnerability of ice sheets to even relatively low levels of sustained global warming.

METHODS SUMMARY

We assembled our database, which includes observations from 42 localities, through an extensive literature search for indicators with best estimates of ages between 140 and 90 kyr ago. To each indicator we assigned a depth range of formation or deposition based upon geomorphological and sedimentological interpretation. See Methods and Supplementary Information for full details of the database, the statistical analysis algorithm, and the physical model used to generate the covariance function.

Full Methods and any associated references are available in the online version of the paper at www.nature.com/nature.

1. Jansen, E. *et al.* in *Climate Change 2007: The Physical Science Basis* (eds Solomon, S. *et al.*) 433–498 (Cambridge Univ. Press, 2007).
2. Meehl, G. A. *et al.* in *Climate Change 2007: The Physical Science Basis* (eds Solomon, S. *et al.*) 747–845 (Cambridge Univ. Press, 2007).
3. Rahmstorf, S. A semi-empirical approach to projecting future sea-level rise. *Science* **315**, 368–370 (2007).
4. Grinsted, A., Moore, J. C. & Jevrejeva, S. Reconstructing sea level from paleo and projected temperatures 200 to 2100 AD. *Clim. Dyn.* doi:10.1007/s00382-008-0507-2 (published online 6 January 2009).
5. Cuffey, K. M. & Marshall, S. J. Substantial contribution to sea-level rise during the last interglacial from the Greenland ice sheet. *Nature* **404**, 591–594 (2000).
6. Otto-Bliesner, B., Marshall, S., Overpeck, J., Miller, G. & Hu, A. Simulating Arctic climate warmth and icefield retreat in the Last Interglaciation. *Science* **311**, 1751–1753 (2006).
7. Petit, J. *et al.* Climate and atmospheric history of the past 420,000 years from the Vostok ice core, Antarctica. *Nature* **399**, 429–436 (1999).
8. Berger, A. & Loutre, M. F. Insolation values for the climate of the last 10 million years. *Quat. Sci. Rev.* **10**, 297–317 (1991).
9. Crowley, T. & Kim, K. Milankovitch forcing of the Last Interglacial sea level. *Science* **265**, 1566–1568 (1994).
10. Katsov, V. M. *et al.* in *Arctic Climate Impact Assessment* (eds Symon, C., Arris, L. & Heal, B.) Ch. 4, 99–150 (Cambridge Univ. Press, 2004).
11. Kaspar, F., Kühl, N., Cubasch, U. & Litt, T. A model-data comparison of European temperatures in the Eemian interglacial. *Geophys. Res. Lett.* **32**, L11703, doi:10.1029/2005GL022456 (2005).
12. Lea, D. The 100,000-yr cycle in tropical SST, greenhouse forcing, and climate sensitivity. *J. Clim.* **17**, 2170–2179 (2004).
13. Weldeab, S., Lea, D., Schneider, R. & Andersen, N. 155,000 years of West African monsoon and ocean thermal evolution. *Science* **316**, 1303–1307 (2007).
14. Farrell, W. E. & Clark, J. A. On postglacial sea level. *Geophys. J. R. Astron. Soc.* **46**, 647–667 (1976).
15. Mitrovica, J. X. & Milne, G. A. On post-glacial sea level: I. General theory. *Geophys. J. Int.* **154**, 253–267 (2003).
16. Kendall, R., Mitrovica, J. & Milne, G. On post-glacial sea level – II. Numerical formulation and comparative results on spherically symmetric models. *Geophys. J. Int.* **161**, 679–706 (2005).
17. Yin, J., Schlesinger, M. E. & Stouffer, R. J. Model projections of rapid sea-level rise on the northeast coast of the United States. *Nature Geosci.* **2**, 262–266 (2009).
18. Mitrovica, J. X. & Milne, G. A. On the origin of late Holocene sea-level highstands within equatorial ocean basins. *Quat. Sci. Rev.* **21**, 2179–2190 (2002).
19. Lambeck, K. & Nakada, M. Constraints on the age and duration of the last interglacial period and on sea-level variations. *Nature* **357**, 125–128 (1992).
20. Lisiecki, L. E. & Raymo, M. E. A Pliocene-Pleistocene stack of 57 globally distributed benthic δ^{18}O records. *Paleoceanography* **20**, 1–17 (2005).
21. Zagwijn, W. H. Sea-level changes in the Netherlands during the Eemian. *Geol. Mijnb.* **62**, 437–450 (1983).
22. Rohling, E. J. *et al.* High rates of sea-level rise during the last interglacial period. *Nature Geosci.* **1**, 38–42 (2008).
23. Mitrovica, J., Wahr, J., Matsuyama, I. & Paulson, A. The rotational stability of an ice-age earth. *Geophys. J. Int.* **161**, 491–506 (2005).
24. Peltier, W. R. Global glacial isostasy and the surface of the ice-age Earth: the ICE-5G (VM2) model and GRACE. *Annu. Rev. Earth Planet. Sci.* **32**, 111–149 (2004).
25. Banerjee, S., Carlin, B. P. & Gelfand, A. E. *Hierarchical Modeling and Analysis for Spatial Data* (Chapman & Hall/CRC, 2003).
26. Lighty, R. G., Macintyre, I. G. & Stuckenrath, R. *Acropora palmata* reef framework: a reliable indicator of sea level in the western Atlantic for the past 10,000 years. *Coral Reefs* **1**, 125–130 (1982).
27. Camoin, G. F., Ebren, P., Eisenhauer, A., Bard, E. & Faure, G. A 300,000-yr coral reef record of sea level changes, Mururoa atoll (Tuamotu archipelago, French Polynesia). *Palaeogeogr. Palaeoclimatol. Palaeoecol.* **175**, 325–341 (2001).
28. Rasmussen, C. & Williams, C. *Gaussian Processes for Machine Learning* (MIT Press, 2006).
29. Hastings, W. K. Monte Carlo sampling methods using Markov chains and their applications. *Biometrika* **57**, 97–109 (1970).
30. Muhs, D. R., Simmons, K. R. & Steinke, B. Timing and warmth of the Last Interglacial period: new U-series evidence from Hawaii and Bermuda and a new fossil compilation for North America. *Quat. Sci. Rev.* **21**, 1355–1383 (2002).
31. Overpeck, J. T. *et al.* Paleoclimatic evidence for future ice-sheet instability and rapid sea-level rise. *Science* **311**, 1747–1750 (2006).
32. Schellmann, G. & Radtke, U. A revised morpho- and chronostratigraphy of the Late and Middle Pleistocene coral reef terraces on Southern Barbados (West Indies). *Earth Sci. Rev.* **64**, 157–187 (2004).
33. Esat, T. M., McCulloch, M. T., Chappell, J., Pillans, B. & Omura, A. Rapid fluctuations in sea level recorded at Huon Peninsula during the penultimate glaciation. *Science* **283**, 197–202 (1999).
34. Carlson, A. E. *et al.* Rapid early Holocene deglaciation of the Laurentide ice sheet. *Nature Geosci.* **1**, 620–624 (2008).
35. Tamisiea, M. E., Mitrovica, J. X. & Davis, J. L. GRACE gravity data constrain ancient ice geometries and continental dynamics over Laurentia. *Science* **316**, 881–883 (2007).

Author Contributions R.E.K. compiled the database, developed the statistical analysis method, and co-wrote the paper. F.J.S. contributed to the development of the statistical analysis method and co-wrote the paper. J.X.M. developed the physical sea level model and co-wrote the paper. A.C.M. contributed to the compilation of the database and co-wrote the paper. M.O. supervised the project and co-wrote the paper.

Author Information Reprints and permissions information is available at www.nature.com/reprints. The authors declare no competing financial interests. Correspondence and requests for materials should be addressed to R.E.K. (rkopp@alumni.caltech.edu).

METHODS

Database of LIG sea level indicators. We characterize each LIG sea level indicator (indexed by i) by five parameters: its geographical position ($\mathbf{r}_i$), its measured altitude with respect to mean tide level (z_i), its measured age (t_i), the range of depths at which it might have formed ($\mathbf{D}_i$), and the estimated local uplift or subsidence rate (u_i). Some of the observations are censored, in that they provide only an upper or lower bound to sea level. When more than one observation comes from the same locality, we also record stratigraphic order and, where available, estimates of the relative ages of observations. With the exception of geographical position, each of these variables has uncertainties that we assume follow a Gaussian distribution. For some values, including all depositional depth ranges, uniform distributions between two limits a and b may be a better choice than Gaussian ones. In these cases, we substitute a Gaussian distribution with the same mean and standard deviation as the uniform distribution, that is, $(b-a)/\sqrt{12}$. Depositional ranges $\mathbf{D}_i$ are thus replaced with Gaussian estimates d_i. The full database is supplied in Supplementary Information.

Prior distribution. We assume that sea level is a Gaussian process with a spatially and temporally varying covariance described by the function $k(\mathbf{r}_i, g_i; \mathbf{r}_j, g_j)$. There is no uncertainty on spatial location $\mathbf{r}_i$, but the temporal variable is g_i, the model age (see Fig. 3). We approximate k by $\hat{k}$, which is produced by sampling alternative histories from a forward model that incorporates the relevant physics. To stabilize the estimate and reduce variability related to finite sample size, we smooth $\hat{k}$ with a Gaussian temporal taper function: $\hat{k}(\mathbf{r}_i, g_i ; \mathbf{r}_j, g_j) = \hat{k}_0(\mathbf{r}_i, g_i; \mathbf{r}_j, g_j) \exp\left[-(g_i - g_j)^2/\tau^2\right]$, as discussed in the Supplementary Information. To produce the results described in the main text, we employed $\tau = 3$ kyr. Results from other values are shown in Supplementary Information.

The prior probability distribution is based upon the age model of ref. 20, which places the start of the deglaciation at about 135 kyr ago and the start of the LIG highstand at about 127 kyr ago. For consistency, we have aligned the Red Sea and Dutch sequences against this record and excluded from the main analysis three observations from the Houtman-Abrolhos Islands[36,37] whose ages are inconsistent with this model. There is, however, considerable disagreement among current age models. Reference 38 (adopted in ref. 22) places the start of the highstand at about 125 kyr ago, 2 kyr later than ref. 20, while ref. 39 places the start of the deglaciation at between 137 and 142 kyr ago, 2–7 kyr earlier. Our results do not attempt to address these differences, and should be viewed in the context of the ref. 20 timescale.

Physical model. The physical model is based on a gravitationally self-consistent sea-level equation[15] that extends earlier work[14] to take exact account of shoreline migration due to either local sea-level changes (which give rise to offlap or onlap) and changes in the extent of grounded, marine-based ice. The calculations are performed using a pseudo-spectral sea-level solver[16,40] with a truncation at spherical harmonic degree and order 256. The solver incorporates the feedback on sea level of contemporaneous, load-induced perturbations in the Earth's rotation vector[16], where these perturbations are computed using the new ice-age rotation theory of ref. 23. The sensitivity to Earth structure is embedded within viscoelastic surface load and tidal Love numbers[41,42]. We adopt spherically symmetric, self-gravitating, Maxwell viscoelastic Earth models. The elastic and density structure of these models is given by the seismic model PREM (ref. 43). The viscosity profile is discretized into three layers, including: (1) an extremely high (essentially elastic) lithospheric lid of thickness LT; (2) a uniform viscosity from the base of the lithosphere to 670 km depth (that is, the sub-lithospheric upper mantle) which we denote as ν_{UM}; and (3) a uniform lower mantle viscosity (that is, from 670 km depth to the core-mantle boundary) denoted by ν_{LM}. We consider a suite of 72 such Earth models generated by using the following choices: LT = 70, 95, or 120 km; ν_{UM} = 0.3, 0.5, 0.8 or 1.0×10^{21} Pa s; ν_{LM} = 2, 3, 5, 8, 10, or 20×10^{21} Pa s.

As described in Supplementary Information, we generate an estimate of the prior sea level covariance $\hat{k}$ by running the model 250 times with different ice sheet histories and randomly selected viscosity profiles. From these runs, we compute the covariance among LSLs at evenly spaced points, GSLs and ice sheet volumes, as well as at the exact coordinates of the sites in our database, and we store the results as a lookup table. Total ice volume in the different ice sheet histories is sampled from a distribution based upon the ref. 20 global oxygen isotope curve. The ice volume of individual ice sheets is sampled from a probability distribution for individual ice sheet volumes that is conditional upon total global ice volume. This latter distribution is constructed from random perturbations of LGM-to-present ice models[24].

36. Eisenhauer, A., Zhu, Z., Collins, L., Wyrwoll, K. & Eichstätter, R. The Last Interglacial sea level change: new evidence from the Abrolhos islands, West Australia. *Int. J. Earth Sci.* **85,** 606–614 (1996).

37. Zhu, Z. R. *et al.* High-precision U-series dating of Last Interglacial events by mass spectrometry: Houtman Abrolhos Islands, western Australia. *Earth Planet. Sci. Lett.* **118,** 281–293 (1993).

38. Thompson, W. G. & Goldstein, S. L. Open-system coral ages reveal persistent suborbital sea-level cycles. *Science* **308,** 401–405 (2005).

39. Thomas, A. L. *et al.* Penultimate deglacial sea-level timing from uranium/thorium dating of Tahitian corals. *Science* **324,** 1186–1189 (2009).

40. Mitrovica, J. X. & Peltier, W. R. On postglacial geoid subsidence over the equatorial ocean. *J. Geophys. Res.* **96,** 20053–20071 (1991).

41. Peltier, W. R. The impulse response of a Maxwell Earth. *Rev. Geophys. Space Phys.* **12,** 649–669 (1974).

42. Wu, P. *The Response of a Maxwell Earth to Applied Surface Mass Loads: Glacial Isostatic Adjustment.* M.Sc. thesis, Univ. Toronto (1978).

43. Dziewonski, A. & Anderson, D. Preliminary reference Earth model. *Phys. Earth Planet. Inter.* **25,** 297–356 (1981).

Supplementary Methods: Database Compilation

Nature of the indicators and depositional ranges. The sea level indicators take a variety of forms, including: constructional coral terraces that provide both geomorphological and ecological information; coral biofacies in limestones that provide ecological but not geomorphological information; erosional features such as wave-cut terraces, sea caves, bioerosional notches, and raised beaches; and sedimentological and biofacial indicators of depositional depth.

Most of the indicators reflect deposition or formation within a specific range of depths. The most common reef terraces and associated coral assemblages, for instance, are generally interpreted as indicating deposition between mean low tide level and 5 m below mean low tide level[1,2]. Intertidal sedimentary facies indicate deposition within the tidal range. While recognizing that LIG tidal amplitudes could have been slightly different than today, we convert descriptive ranges such as these into a common reference frame based on the tidal ranges reported in tide tables at a nearby modern locality. We also attempt to correct for variability in the measurement datum; while most sea level indicators have altitudes reported with respect to "modern sea level", some are more usefully described with reference to datums such as the mean low tide level or mean high tide level. We convert such datums into a mean tide level datum.

Some data, such as subtidal sedimentary facies, are limiting points; they place an upper or lower limit on past sea level but do not indicate a specific depositional depth. In statistical terminology, limiting points are censored data.

Age. Age constraints on our data come from a variety of sources with a range of precisions. In some cases, age is constrained only by stratigraphic relationships with other units. In many cases, particularly involving coral reefs, radiometric (U/Th) dates are available. Other age constraints are derived from amino acid racemization, electron spin resonance dating, and related techniques such as thermoluminescence.

In three cases (the global oxygen isotope curve, the Red Sea oxygen isotope curve, and the Dutch sea level curve), relative ages are known with more precision than absolute ones. As described below, we

have scaled and shifted the age models of the Red Sea and Dutch local sea level curves to be consistent with the Lisiecki and Raymo[3] age model for the global oxygen isotope curve. All of the dates outputted by our analysis should therefore be viewed within the context of this age model, which places the start of the Penultimate Termination at 135 ka and the peak of the Last Interglacial at about 122–126 ka.

When only a single conventional U/Th measurement from a unit is available, we expand the quoted ranges by 350%, following the empirical observation of Scholz et al.[4] of the overestimate of the precision of ages from single-sample measurements. When multiple measurements are reported, we employ their inverse-variance weighted mean. We expand the inverse-variance weighted standard deviation using a Student's t-distribution so that the 95% confidence interval spans $\pm 1.96\sigma$, with σ the standard deviation, as in a Gaussian distribution.

Tectonic uplift or thermal subsidence rate. In order to remove the local tectonic contribution to paleo-sea level, we seek locally calibrated subsidence or uplift estimates for each locality. For most of the points in our database, no estimate of uplift or subsidence is available, but the value is expected to be near zero for short (~ 100 ky) time scales. For these locations, we adopt an estimate of 0 ± 1 cm/ky. (For subsiding localities, this is conservative with regards to peak sea level, as underestimates of subsidence will lead to sea level underestimates.) In a few regions where estimates are available, including much of the Bahamas and Hawai'i, subsidence or uplift is on the order of 1–2 cm/ky. A few localities have exhibited uplift (Barbados, Patagonia, southern England) or subsidence (the Netherlands, Pacific and Indian Ocean atolls) in excess of about 10 cm/ky. The fastest uplifting locality in our database, Barbados, is rising at about 28 cm/ky.

Coverage. Our database attains fairly good geographic coverage, including the northwestern, northeastern, and southwestern Atlantic coasts; the Carribean; Alaska, Greenland, Svalbard, and Siberia; Australia; the southwestern Indian coast; and Pacific and Indian Ocean islands (Figures 1 and 3; Table S1). Where nearby localities subject to less uplift are available, we have tried to limit the amount of data from rapidly uplifting sites, though we include Barbados because of its prominence in the literature. However, given the long history of the geological study of Pleistocene sea level indicators , which began not long after the collapse of the Diluvian hypothesis in the early nineteenth century[5], we do not claim that our database comprehensively represents the entire literature.

Supplementary Methods: Database

The database is recorded in a spreadsheet that accompanies this Supplementary Information. Two of the sites are re-analyses of data available elsewhere that require special explanations: the re-aligned Red Sea sea level curve of Rohling et al.[6] and a subsidence-corrected Dutch sea level curve based on the work of Zagwijn[7].

Red Sea. The Red Sea record is a planktonic foraminiferal oxygen isotope record that, because of the hydrological structure of the sea[8], is essentially a record of local sea level at the strait of Bab-el-Mandeb. The oxygen isotopic composition of Red Sea water is controlled primarily by evaporation. Water exchange between the Red Sea and the Indian Ocean occurs through the strait; when sea level is lower, water exchange decreases, which increases the residence time of water in the Red Sea and thus yields heavier oxygen isotope values. This greatly magnifies the isotopic effects of sea level change. The difference between the modern and the Last Glacial Maximum in the Red Sea is nearly 6‰, whereas in the open ocean the difference is approximately 1.8‰.

Using a hydrological model, Rohling et al.[6] constructed a sea level record with a raw 1σ precision of 6 m for the Last Interglacial from two Red Sea cores sampled for oxygen isotopes at 10 cm resolution. They aligned their record temporally with the record derived from U/Th-dated Barbados coral data[9]; in this age model, their record has a temporal resolution of 200–400 years. It indicates that local sea level rose to at least 6 ± 3.5 m, and perhaps as high as 11 m, during the peak interglacial.

We have for consistency realigned the Red Sea curve against the age model for the global oxygen isotope stack[3], which is based primarily on alignment against the GRIP ice core. This realignment required shifting the curve earlier by 2.4 ka and expanding the duration between measurements 1.2 times. We include in our database the re-aligned sea level curve derived from the KL11 core, which Rohling et al. argue provides a higher resolution record than the KL09 core.

Netherlands. The Dutch Eemian sea level record of Zagwijn[7] is based on sedimentological and micropale-ontological data from numerous cores through the Amsterdam and Amersfoort basins, as well as cores along

the Noord-Holland coast, in Friesland, and in the North Sea. Sea level indicators in these cores are provided by facies transitions representing, for example, the infiltration of marine water into a freshwater lake or the maximum elevation of clays deposited in a salt-marsh environment. Relative age constraints are provided by characteristic Eemian pollen zones, many of which have durations established to fairly high precision based upon the counting of varves in an annually-layered lacustrine diatomite in northwestern Germany[10]. We place peak sea level in the middle third of zone E5 based upon the position of the maximum flooding interval within the more recent Amsterdam-Terminal borehole[11]. We estimate absolute ages from these relative ages by aligning the sea level curve against the global oxygen isotope stack.

Zagwijn reported sea level estimates without correction for long-term isostasy, compaction, or tectonics. To correct for these factors, we use the backstripping-derived Quaternary rate estimates of Kooi et al.[12]. These vary considerably across the Netherlands and the North Sea, ranging from about 12 cm/ky in Amersfoort to about 18 cm/ky in Petten. Thus adjusted, Zagwijn's data indicate that a maximum local sea level of about 5 ± 2 m was attained in the Netherlands for much of the Last Interglacial.

Supplementary Methods: Statistical Model

Preliminaries and Notation. The ultimate goal of our statistical analysis is to determine the posterior probability distribution of sea level through time, conditioned upon the measurements in our database. Expressed symbolically, our aim is to evaluate the probability $P(f(\mathbf{x}, g)|\mathbf{r}, \mathbf{z}, \mathbf{t}, \mathbf{D}, \mathbf{u})$ for locations $\mathbf{x}$ on Earth's surface and times g, where f represents the true value of sea level at $\mathbf{x}$ and g. In our database, each sea level indicator is assigned an index $i = 1, \ldots, N$ and is characterized by

$\mathbf{r}_i$, its exact geographic position,

z_i, a noisy measurement of its altitude,

t_i, a noisy measurement of its age,

$\mathbf{D}_i$, a closed or open interval reflecting its depositional range, and

u_i, a noisy estimate of the long-term average uplift or subsidence rate.

When $\mathbf{D}_i$ is a closed interval, we replace it with d_i, a Gaussian estimate of depositional depth characterized by the same mean and variance as the uniform distribution on $\mathbf{D}_i$, as discussed in the Methods section.

We collect these parameters into vectors $\mathbf{r}$, $\mathbf{z}$, $\mathbf{t}$, $\mathbf{D}$, $\mathbf{u}$, and $\mathbf{d}$. Similarly, we collect what will be the true sea levels in a vector $\mathbf{f}$ evaluated at the times $\mathbf{g}$ and locations $\mathbf{x}$, whose elements f_j, g_j and $\mathbf{x}_j$ for $j = 1, \ldots, M$ are the desired sea levels and evaluation points. Only when geographical positions and depositional ranges are concerned does the bold vector notation serve double-duty: $\mathbf{x}$ and $\mathbf{r}$ are either coordinates or vectors of coordinates, and $\mathbf{x}_i$, $\mathbf{r}_i$ and $\mathbf{x}_j$, $\mathbf{r}_j$ are individual sets of coordinates. Likewise, $\mathbf{D}$ is either a depositional range or an array of depositional ranges, and $\mathbf{D}_i$ is an individual depositional range. This dual purpose is not, however, likely to lead to confusion.

Gaussian process regression. We proceed from this point using a Gaussian process approach[13]. We must select some covariance function for true sea level, $k(\mathbf{r}_i, g_i; \mathbf{r}_j, g_j)$, as we will address below. Let $(\mathbf{f}, \mathbf{g})$ refer to the vectors of true sea levels and ages that correspond to the vectors of measurements $(\mathbf{z}, \mathbf{t}, \mathbf{D}, \mathbf{u})$; i.e., with every entry (f_i, g_i), we associate an entry $(z_i, t_i, \mathbf{D}_i, u_i)$ for all indices $i = 1, \ldots, N$. With the covariance function k given, we can then readily recover an estimate of true sea level at any arbitrary location $\mathbf{x}'$ and time g' through straight-forward kriging interpolation[14]. We denote the mean and variance of this estimate by $\overline{f}(\mathbf{x}', g')$ and $\mathbf{V}(f(\mathbf{x}', g'))$, respectively.

As before, the vectors $\overline{\mathbf{f}}$, $\mathbf{x}'$ and $\mathbf{g}'$ will collect the mean estimates of the sea levels at the desired points $\mathbf{x}'$ and $\mathbf{g}'$ in space and time. The sets of desired evaluation points $(\mathbf{x}'_j, g'_j)$, $j = 1, ..., M$, and the measurements $(\mathbf{r}_i, g_i)$, $i = 1, ..., N$ need not necessarily overlap. The matrix $\mathbf{V}''$ collects the kriging (co)variance of $\mathbf{f}'$ at and between $(\mathbf{x}', \mathbf{g}')$. Let $\mathbf{K}$, $\mathbf{K}'$, and $\mathbf{K}''$ be the covariances of $(\mathbf{f}, \mathbf{g})$ and/or $(\mathbf{f}', \mathbf{g}')$ at the observed and desired points, i.e., let the symmetric square matrices $\mathbf{K}$ and $\mathbf{K}''$ and the rectangular matrix $\mathbf{K}'$ be defined by their elements:

$$K_{ij} = k(\mathbf{r}_i, g_i; \mathbf{r}_j, g_j) \qquad \text{where } i, j = 1, ..., N, \qquad (\text{S1})$$

$$K''_{ij} = k(\mathbf{x}'_i, g'_i; \mathbf{x}'_j, g'_j) \qquad \text{where } i, j = 1, ..., M, \qquad (\text{S2})$$

$$K'_{ij} = k(\mathbf{r}_i, g_i; \mathbf{x}'_j, g'_j) \qquad \text{where } i = 1, ..., N \text{ and } j = 1, ..., M. \qquad (\text{S3})$$

From this, the kriging step consists of calculating $\overline{\mathbf{f}}$, the $M \times 1$ vector of mean sea level estimates at $(\mathbf{x}', \mathbf{g}')$,

as

$$\overline{\mathbf{f}} = \mathbf{K}'^{\top} \mathbf{K}^{-1} \mathbf{f}, \qquad (\text{S4})$$

which has

$$\mathbf{V}'' = \mathbf{K}'' - \mathbf{K}'^{\top} \mathbf{K}^{-1} \mathbf{K}' \qquad (\text{S5})$$

as its $M \times M$ covariance matrix. It is clear from the above that, when $\mathbf{x}' = \mathbf{r}$ and $\mathbf{g}' = \mathbf{g}$, $\mathbf{K} = \mathbf{K}' = \mathbf{K}''$,

and therefore $\overline{\mathbf{f}} = \mathbf{f}$ and $\mathbf{V}'' = \mathbf{0}$. In other words, when the queried points are identical to the measurement

locations, the interpolated values of true sea level remain unchanged and receive no kriging variance.

We can therefore replace the problem of finding the posterior probability of sea level anywhere,

$P(f(\mathbf{x}, g)|\mathbf{r}, \mathbf{z}, \mathbf{t}, \mathbf{D}, \mathbf{u})$, with the more tractable problem of finding $P(\mathbf{f}, \mathbf{g}|\mathbf{z}, \mathbf{t}, \mathbf{D}, \mathbf{u})$, which is the posterior

probability of sea level at the smaller set of points defined by the measurement locations. After adjusting

altitude z_i for uplift or subsidence rate u_i over a time g_i, we define the corrected altitude z'_i as

$$z'_i \equiv z_i - g_i u_i, \qquad (\text{S6})$$

with variance

$$\sigma_{z'i}^2 \equiv \sigma_{zi}^2 + g_i^2 \sigma_{ui}^2, \tag{S7}$$

and we define the sea level measurement s_i and its variance σ_{si}^2 as

$$s_i \equiv z_i' - d_i, \tag{S8}$$

$$\sigma_{si}^2 \equiv \sigma_{z'i}^2 + \sigma_{di}^2, \tag{S9}$$

where σ_{zi}^2, σ_{ui}^2, and σ_{di}^2 are the variances respectively of altitude z_i, uplift rate u_i, and depositional depth d_i.

By Bayes' theorem,

$$P(\mathbf{f}, \mathbf{g}|\mathbf{s}, \mathbf{t}) \propto P(\mathbf{s}, \mathbf{t}|\mathbf{f}, \mathbf{g}) \cdot P(\mathbf{f}, \mathbf{g}). \tag{S10}$$

We drop the position variable $\mathbf{r}$ from the notation, since its values are fixed in the data set and implicit in the indexing of the other variables. For uncensored sea level measurements, we have the likelihood

$$P(s_i|f_i, g_i) \sim \mathcal{N}(f_i, \sigma_{si}^2). \tag{S11}$$

In other words, the probability of observing sea level s_i at a point in the data set that has a true sea level of f_i is given by a Gaussian centered on the truth with variance σ_{si}^2. For censored data,

$$P(s_i|f_i, g_i) \sim \mathcal{N}(f_i, \sigma_{si}^2) \cdot \delta\big((z_i' - s_i) \in \mathbf{D}_i\big) \tag{S12}$$

where δ is an indicator function that is 1 when $z_i' - s_i$ is in the depositional range $\mathbf{D_i}$ and 0 otherwise. For instance, if $\mathbf{D}_i$ is $(-\infty, -2]$, reflecting deposition at least two meters below mean tide level, then δ would be 1 for $s_i \geqslant z_i' + 2$ and 0 otherwise. For age measurements, we have the likelihood

$$P(t_i|g_i) \sim \mathcal{N}(g_i, \sigma_{ti}^2), \tag{S13}$$

where σ_{ti}^2 is the variance of age measurement t_i. For the sea level vector $\mathbf{f}$, we compute a prior of the form

$$P(\mathbf{f}|\mathbf{g}) \sim \mathcal{N}(\mu(\mathbf{g}), \mathbf{K}(\mathbf{g})), \tag{S14}$$

as discussed below, where we use the notation $\mu(\mathbf{g})$ and $\mathbf{K}(\mathbf{g})$ for the covariance to emphasize the dependence of the mean and covariance not just on locations $\mathbf{r}$ but also on ages $\mathbf{g}$. For the age vector $\mathbf{g}$ itself, we assume a uniform prior.

Prior distribution for sea level and ice volume. The prior distribution for sea level and ice volume is based upon the global oxygen isotope curve of ref. 3 and is determined through a five step process. First, we construct a multivariate Gaussian distribution for total global ice volume through time based upon the oxygen isotope curve. Second, we construct a distribution for the volume of each major ice sheet and Northern and Southern Hemisphere glaciers conditioned upon total global ice volume. Third, we sample 250 alternative ice sheet histories from these distributions and use a physical model to determine the associated local sea levels. Fourth, we add a thermosteric component of sea level to each alternative history. Finally, we compute the mean and covariance of local sea level, global sea level, and ice sheet volumes as a function of space and time from these alternative histories. The spatial covariance of local sea level with global sea level at two illustrative time points and the temporal covariance of global sea level are shown in Figures S4 and S5.

Distribution of global ice volume over time. The distribution of global ice volume over time is based upon the global oxygen isotope curve of ref. 3. First, we note that the difference in $\delta^{18}O$ between the present value ($\delta_0 = 3.23 \pm 0.03‰$) and the peak Last Glacial Maximum ($5.02 \pm 0.03‰$ at 18 ka) is $1.79 \pm 0.04‰$ and is associated with a change in sea level of about 125 m (ref. 15). Assuming a simple linear relationship between $\delta^{18}O$ and global ice volume yields a proportionality constant c of about 70 m/‰. Ref. 16 notes, however, that there is considerable deviation from a simple linear relationship; their results indicate that this assumption can give rise to an inaccuracy of as much as 20 m. We therefore assume that global ice volumes

derived from this scaling factor have a 1σ uncertainty of ± 10 m in addition to any uncertainty arising from measurement imprecision. From this relationship, we derive mean predictions for total global ice volume and the diagonal terms of the associated covariance matrix: at time i, where $\Delta_i = \delta_i - \delta_0$, the mean ice volume prediction $\overline{I_i} = c\Delta_i$ and its variance $\sigma_{I_i}^2 = c^2 \sigma_{\Delta_i}^2 + 100$.

To determine the off-diagonal terms, we note that changes in global ice volume are constrained by changes in the global oxygen isotope curve: $I_i - I_j = (c \pm \sigma_c)(\delta_i - \delta_j)$ where $I_{i,j}$ are global ice volumes at times i and j, c is the proportionality constant between global ice volume and oxygen isotope values, σ_c is the standard deviation of c, and $\delta_{i,j}$ are the values of the oxygen isotope curve at times i and j. As noted previously, we use $c = 70$ m/‰, but also note that at values of δ close to the present value, the proportionality constant can vary by as much as about 70%[16]. We therefore use $\sigma_c = 25$ m/‰. The covariance of I_i and I_j is given by $0.5 \times (\sigma_{I_i}^2 + \sigma_{I_j}^2 - \sigma_{I_i-I_j}^2)$, where $\sigma_{I_i-I_j}^2 = \sigma_c^2(\Delta_i - \Delta_j)^2 + c^2(\sigma_{\Delta_i}^2 + \sigma_{\Delta_j}^2)$.

Because c changes over time, we apply a Gaussian taper with a standard deviation of 3 ka to the covariance. The covariance between global ice volume at times i and j is thus given by $c_I(i,j) = 0.5 \times e^{-\left(\frac{i-j}{5}\right)^2} \times (\sigma_{I_i}^2 + \sigma_{I_j}^2 - \sigma_{I_i-I_j}^2)$. (The resulting distribution is shown in Figures S1 and S2.)

Distribution of ice sheet volumes conditional upon global ice volume. To determine the distribution of ice sheet volumes conditional upon global ice volume, we start with two alternative reconstructions of LGM-to-present ice sheet volumes[15], distinguishing between five ice sheets – Laurentide, Scandinavian, Greenland, West Antarctic and East Antarctic – as well as northern and southern hemisphere glaciers. From each base model, we generate approximately 8000 random perturbations by multiplying the change in each ice sheet's volume between each time step by a random log normal factor with a log standard deviation of 3×. We similarly multiply the change in total ice volume between each time step by a random log normal factor with a log standard deviation of 1.5× and then multiply the ice sheet volumes by a correction factor that maintains the proportional distribution of ice volume among the ice sheets while ensuring that ice volumes add to the correct value. We also add cases with additional mass loss from the ice sheets, in

which total ice volume shrinks below its present value. We then bin by total ice volume to generate the desired distribution (Figure S3). Note that this distribution is a function of global ice volume, not of time. When sampling ice sheet volume over time, we impose a weak constraint on the rate of change of ice sheet volumes so as to prevent wild oscillations in ice distribution during intervals of little change in total ice volume. To turn a numerical quantity reflecting the total volume in ice sheet into a geographical map of land ice, we scale the map from the timeslice of the ICE-5G LGM-to-present reconstruction[15] that is closest to but not smaller than the desired volume.

Alternative histories for physical modeling. We draw 250 samples from the distribution for global ice volume. To account for uncertainty in the dating of the global oxygen isotope curve, we keep one time point (120 ka) fixed as an anchor for our age model and allow the nominal 1-ky spacing between oxygen isotope measurements to vary with a standard deviation of 250 y. We then interpolate to get evenly spaced measurements and subsequently draw associated ice sheet histories from the distribution described above. The 250 alternative histories thus calculated serve as inputs to the physical model described in the Methods section, which is based on the gravitationally self-consistent sea-level equation derived by Mitrovica et al.[17] and calculates local sea levels for each history.

For each history, we also estimate an associated thermosteric change in sea level. Based upon the projections for year 3000 thermal expansion summarized by ref. 18, we estimate a relationship between temperature and thermosteric sea level of about 0.39 ± 0.14 m/°C. Assuming that the ~ 125 m equivalent sea level of global ice volume change between the LGM and present was associated with ~ 5°C of cooling yields about -1.55 ± 0.57 cm of thermal contracting per meter ice volume growth. To allow the thermosteric component of sea level to change without much accompanying ice volume change, we add an additional ice volume-independent thermosteric term with a mean of zero, a standard deviation of 2 m, and a Gaussian temporal covariance with a standard deviation of 2 ky (Figure S2).

We explicitly calculate the mean and covariance for sea level and ice volume over time from these

alternative histories, which we then store as a lookup table. We use linear interpolation over time to provide continuity. For computational efficiency, we perform these operations using a principal component decomposition of sea level and retain sufficient principal components to account for 99% of the variance. This reduces an computationally nearly intractable 71,350 x 71,350 covariance matrix to an easily tractable 177 x 177 covariance matrix. For time points that fall outside the principal time range of interest (149–100 ka), we use a spatial mean and covariance that combines results across all time points.

Temporal taper function. To reducing sampling-associated noise in the covariance function, we employ a Gaussian temporal taper function as described in the Methods section. We tested four different values for the standard deviation τ of this taper function: 2 ky, 3 ky, 4 ky, and ∞ (i.e., no taper). The resulting GSL projections are shown in Figure S9 and summary statistics are shown, alongside summary statistics for different data subsets, in Table S2. We adopted a 3 ky taper for the main analysis.

Algorithm for sampling the posterior sea level distribution. To explore the distribution in equation S10, we use a three-step Gibbs sampler that in turn calculates $p(s|g)$, $p(f|s,g)$ and $p(g|f)$. We start by initializing $\mathbf{g} = \mathbf{t}$ for all data points and $z_i' = z_i - g_i u_i$ and $f_i = s_i = z_i' - d_i$ for the uncensored ones. By simple kriging interpolation (equations S4 and S5), we estimate f_i at the remaining data points.

1. In step one of our algorithm, we calculate values of sea level measurements $\mathbf{s}$ from $\mathbf{z}$, $\mathbf{D}$, $\mathbf{g}$ and $\mathbf{u}$. For uncensored data, s_i is as defined in equation S8. For censored data, we sample s_i from the distribution in equation S12, with an additional variance term σ_{fi}^2, the kriging variance of f_i.

2. In step two, we update our estimate of true sea level $\mathbf{f}$ based upon the new $\mathbf{s}$ as follows. We define the matrix of the sea level measurement noise $\mathbf{N}$, with elements σ_{si}^2 along the diagonal and zero elsewhere. Then, by Gaussian process regression, paralleling equation S4, we calculate

$$\mathbf{f} = \mathbf{K}(\mathbf{g})^\top (\mathbf{K}(\mathbf{g}) + \mathbf{N})^{-1} \mathbf{s}, \tag{S15}$$

the vector of sea level predictions and the vector of their variances

$$\mathbf{\Sigma} = \text{diag}\{\mathbf{K}(\mathbf{g})^\top (\mathbf{I} - (\mathbf{K}(\mathbf{g}) + \mathbf{N})^{-1}\mathbf{K}(\mathbf{g}))\}, \tag{S16}$$

where diag denotes the diagonal elements.

3. In step three, we update our estimate of the true ages $\mathbf{g}$. To do this, we follow a Markov Chain Monte Carlo approach applying the Metropolis-Hastings algorithm sequentially to each g_i. Let $\mathbf{g}_{-i}$ represent $\mathbf{g}$ with element i removed. For each i, we sample from the distribution $P(g_i|\mathbf{t}, \mathbf{g}_{-i}, \mathbf{f})$, which, by multiple applications of Bayes' theorem and the facts that $P(\mathbf{t}|\mathbf{g}) = \prod_i P(t_i|g_i)$ and that $P(\mathbf{t}|\mathbf{f}) = P(\mathbf{t})$, reduces as

$$P(g_i|\mathbf{t}, \mathbf{g}_{-i}, \mathbf{f}) \propto P(t_i|g_i) \cdot P(\mathbf{f}|\mathbf{g}) \cdot P(\mathbf{g}). \tag{S17}$$

The first term is given by equation S13, and the second term by equation S14. We can drop the third term because of our assumption of a uniform prior for $\mathbf{g}$.

We generate test values g_i' using a Gaussian function $q(g_i'; g_i)$ centered at g_i and bounded such that, when stratigraphic ordering is known, a point j that follows a point i always has $g_j \leqslant g_i$. (Where no bounds apply, $q(a; b) = q(b; a)$.) For the sequences where relative ages are known more precisely than absolute ones, these are calculated in terms of time after the preceding point. Following the Metropolis-Hastings algorithm [19], we accept a candidate g_i' with probability

$$\min\left(1, \frac{P(g_i'|\mathbf{t}, \mathbf{g}_{-i}, \mathbf{f}) \cdot q(g_i; g_i')}{P(g_i|\mathbf{t}, \mathbf{g}_{-i}, \mathbf{f}) \cdot q(g_i'; g_i)}\right) = \min\left(1, \frac{P(t_i|g_i') \cdot P(\mathbf{f}|\mathbf{g}_{-i}, g_i') \cdot q(g_i; g_i')}{P(t_i|g_i) \cdot P(\mathbf{f}|\mathbf{g}_{-i}, g_i) \cdot q(g_i'; g_i)}\right). \tag{S18}$$

So that we can assess results within a common temporal reference frame, we arbitrarily set the temporal variance σ_{ti}^2 for the first step of our longest quasi-continuous sequence of data points (the sea level curve derived from the global oxygen isotope stack, for most runs) to zero.

This algorithm, repeated a large number of times, samples the probability distribution described by equation S10. We thin the results by storing every 20th sample and account for burn-in by discarding the

first 50 stored samples. After several parallel executions of the algorithm, each of which store at least about 200 samples, we check for convergence by inspecting the autocorrelation of stored values of $\mathbf{g}$ and discard executions that appear not to converge. To generate our target distribution $P(f(\mathbf{x}, g)|\mathbf{s}, \mathbf{r}, \mathbf{t})$, we use kriging interpolation (equations S1–S5) to estimate the sea level field at all spatial and temporal points of interest for each stored sample.

We note that this algorithm, while satisfying from a theoretical perspective, could benefit from greater computational efficiency. The most time-consuming steps in its execution are the inversions of the covariance matrices, which for a database of n samples require $\mathcal{O}(n^3)$ operations. This inversion occurs once in step 2 and $n + 1$ times in step 3. Thus, each iteration of the algorithm is $\mathcal{O}(n^4)$. Repeating the algorithm a few thousand times in the courses of a Monte Carlo simulation with a database of about 100 points can therefore take a day or more; without increased efficiency, larger data sets will become unmanageable.

Summary statistics for outlier analysis. To identify outliers among the data points, we compute the *probability of a measurement* given the assessed sea level distribution. To do this, we take the average over all N stored MCMC iterations of the probability that the parameter f (local sea level, global sea level, or age) with measured value $f_m \pm \sigma_m$ was drawn from the distribution indicated by iteration i, with mean f_i and standard deviation σ_i. For indicative points, the probability for each iteration is given by a χ^2 distribution with one degree of freedom on the parameter $\frac{(f_i - f_m)^2}{\sigma_i^2 + \sigma_m^2}$. For limiting points, the probability is given by a cumulative normal distribution with mean $f_i - f_m$ and variance $\sigma_i^2 + \sigma_m^2$.

Pseudo-proxy validation analysis. To test our statistical model, we took 20 of the synthetic sea level histories used to generate the prior distribution and sampled them at the same points in space and time and with same chronological and sea-level errors as in the data set. The results show that the algorithm performs more than adequately the task of reconstruction global sea level, rates, and ice volumes (e.g., Figure S6). For these twenty synthetic histories, maximum GSL and GSL rates tend to be slightly higher than expected based on the exceedance values (Figure S7). For instance, while, as expected, in 19 of 20 cases peak GSL

exceeds the 95% exceedance value, in 15 of 20 cases it exceeds the 60% exceedance value (compared to the expected 12 of 20), and in 10 of 20 cases it exceeds the 30% exceedance value (compared to the expected 6 of 20). Given the small number of histories run, a consequence of the computational expense of each analysis, it is not possible to draw general conclusions from this slight apparent low bias.

Supplemental Discussion

Outlier analysis. To search for outliers, we estimated the posterior probabilities for each of our sea level measurements and age measurements given the distribution at each point for sea level and age projected by our statistical model. No data point was a strong outlier, but four sites generated sea level measurement probabilities between 0.10 and 0.33, and four generated age measurement probabilities between 0.11 and 0.30.

First, at Kahe Beach State Park, Oahu, Hawai'i, Hearty et al.[20] describe a marine conglomerate at 12 m above present sea level. Corrected for uplift of Oahu, this suggests a paleo-sea level of at least 9.6 ± 1.3 m. Our model instead assigns a sea level of 7.1 ± 1.5 m, raising the possibility that uplift has been greater than expected.

Second, our model identifies as an outlier early Weichselian (post-Eemian) lacustrine sediment from a boring in the North Sea[7]. The sediment indicates freshwater conditions at a relative sea level of about -40 m, which we adjust to -23 ± 3 m based upon the subsidence estimates of Kooi et al.[12]. The model, however, places sea level at -13.6 ± 5.7 m. This result suggests that the North Sea in the region of this boring is subsiding faster than the estimates.

Third, the model identifies as a marginal outlier a terrace from South Point, Barbados, (terrace T-5b)[21], which has a modern elevation of 41.5 ± 1.7 m and an uplift-corrected paleo-sea level interpretation of 8.1 ± 4.6 m. The model assigns it an elevation of 2.6 ± 3.3 m. Given the high uplift rate in Barbados, this degree of mismatch is unsurprising.

Finally, the model identifies six time points from the Red Sea curve between 124.3 and 118.1 ka as

outliers. At three time points (all with nominal ages between 123.4 and 123.1 ka), the model identifies the data points as overestimates; at three other time points (nominally 124.3, 121.9, and 118.1 ka) the model identifies the data points as underestimates.

The four data points for which the age measurements were marginal outliers were a single coral observation from -1.15 m in the Turtle Bay borehole from East Wallabi Island, Houtman-Abrohlos Islands[23], a 3 m reef terrace from La Digue Island in the Seychelles[44], a 2.4 m exposed reef from Rottnest Island, Australia[39], and a poorly dated 8 m erosional terrace from Aldabra[45]. All four of these identifications are quite marginal; given the uncertainties surrounding the age model, we do not place much stock in them. The Turtle Bay coral has a U-Th age of 129.5 ± 2.6 ka but a model age of 126.6 ka (67% range of 125.9 to 130.8 ka). The La Digue Island reef terrace has a U-Th age of 128.5 ± 3.7 ka but a model age of 125.5 ka (67% range of 124.6 to 130.1 ka). The Rottnest Island reef has a U-Th age of 126.1 ± 1.8 ka but a model age of 125.4 ka (67% range of 124.8 to 130.0 ka). Finally, we assigned the Aldabra terrace a stratigraphic age of 100 ± 35 ka; the model assigns it an age of 120.2 ka (67% range of 115.8 to 123.2 ka).

In addition to these outliers, prior to the primary analysis discussed in the text, we removed three data points that appeared incompatible with our assumed age model. All three points come from the Houtman-Abrohlos Islands[22,23]. The first, a coral at +0.6 m from Mangrove Island, had a reported age of 132.8 ± 0.9 ka. The second, corals from -4.3 m in a bore hole on Rat Island, had a reported age of 134.3 ± 1.3 ka. The third, corals from -3.3 m in a bore hole on Turtle Island, had a reported age of 132.5 ± 1.8 ka. None of the other observations in the database suggested sea levels so close to the modern values at such early ages, and these elevations were clearly incompatible with the oxygen isotope curve used as the basis for the prior. We therefore interpreted these samples as misdated and did not include them.

Need for more data. The ratio of the posterior to prior model covariance is small when the model successfully improves our initial state of knowledge by incorporating the data. Where it remains large, more, or better data, is needed to improve the model. Inasmuch as local data can improve resolution locally, we

can take the value of this ratio to indicate a "data need." While resolution is not a strictly local concept, we define the "data need index" (Figure S10) as the mean of the ratio of the posterior variance to the prior variance over the time period between 114 and 129 ka and plot it over the globe. Because we are particularly interested in sea level near the highstand, we weight the mean by the probability that a sample time slice has global sea level greater than -10 m.

The highest data need is in the near-field and intermediate-field of the major ice sheets. Other areas of high need are fairly widespread along continental coasts. In the far-field of both Northern Hemisphere and Southern Hemisphere ice sheets, the coasts of East and Southeast Asia are notably lacking in the data collection. Unfortunately, acquiring high-precision Asian sea level data for the Last Interglacial will be complicated by the region's active neotectonics.

In compiling the LIG sea level database, we also found a number of regions where sea level indicators require further investigation. For instance, although Britain is on a tectonically stable passive margin, erosional terraces appear to get progressively older with increasing elevation. Westaway et al.[24] estimated Pleistocene uplift rates in the vicinity of the Solent river system range of ~ 10 m/ky. The causes of this uplift are uncertain, but might be linked to isostatic effects caused by erosional unroofing and the transport of sediment from continent to slope. A simple isostatic calculation indicates this method requires the removal of ~ 50 m of sediment per 100 ky. Clayton[25] estimates that an average thickness of ~ 145 m of sediment was removed from the land of the British Isles to the continental shelf during the last glaciation; this removal could therefore be a potential cause. Because the British Isles are in a crucial region to look for the sea-level fingerprint of Greenland melting, a better understanding of regional uplift would be extremely helpful.

Braithwaite[26] described numerous terraces in the coastal limestone of Kenya which range in elevation from -35 m to +20 m but lack good age constraints. These represent ready targets for modern dating techniques.

Supplementary References

1. Lighty, R. G., Macintyre, I. G. & Stuckenrath, R. Acropora palmata reef framework: A reliable indicator of sea level in the western Atlantic for the past 10,000 years. *Coral Reefs* **1**, 125–130 (1982).

2. Camoin, G. F., Ebren, P., Eisenhauer, A., Bard, E. & Faure, G. A 300,000-yr coral reef record of sea level changes, Mururoa atoll (Tuamotu archipelago, French Polynesia). *Palaeogeography, Palaeoclimatology, Palaeoecology* **175**, 325–341 (2001).

3. Lisiecki, L. E. & Raymo, M. E. A Pliocene-Pleistocene stack of 57 globally distributed benthic δ^{18}O records. *Paleoceanography* **20**, 1–17 (2005).

4. Scholz, D. & Mangini, A. How precise are U-series coral ages? *Geochimica et Cosmochimica Acta* **71**, 1935–1948 (2007).

5. Godwin-Austen, R. On the newer Tertiary deposits of the Sussex coast. *Quarterly Journal of the Geological Society* **12**, 4 (1856).

6. Rohling, E. J. *et al.* High rates of sea-level rise during the last interglacial period. *Nature Geoscience* **1**, 38–42 (2008).

7. Zagwijn, W. H. Sea-level changes in the Netherlands during the Eemian. *Geologie en Mijnbouw* **62**, 437–450 (1983).

8. Siddall, M. *et al.* Sea-level fluctuations during the last glacial cycle. *Nature* **423**, 853–858 (2003).

9. Thompson, W. G. & Goldstein, S. L. Open-system coral ages reveal persistent suborbital sea-level cycles. *Science* **308**, 401–405 (2005).

10. Zagwijn, W. H. An analysis of Eemian climate in Western and Central Europe. *Quaternary Science Reviews* **15**, 451–469 (1996).

11. van Leeuwen, R. J. W. *et al.* Stratigraphy and integrated facies analysis of the Saalian and Eemian sediments in the Amsterdam-Terminal borehole, the Netherlands. *Geologie en Mijnbouw* **79**, 161–196 (2000).

12. Kooi, H., Johnston, P., Lambeck, K., Smither, C. & Molendijk, R. Geological causes of recent (100 yr) vertical land movement in the Netherlands. *Tectonophysics* **299**, 297–316 (1998).

13. Rasmussen, C. & Williams, C. *Gaussian processes for machine learning* (MIT Press, Cambridge, MA, 2006).

14. Press, W. H., Teukolsky, S. A., Vetterling, W. T. & Flannery, B. P. *Numerical Recipes: The Art of Scientific Computing* (Cambridge University Press, 2007), third edn.

15. Peltier, W. R. Global glacial isostasy and the surface of the ice-age Earth: The ICE-5G (VM2) model and GRACE. *Annual Review of Earth and Planetary Sciences* **32**, 111–149 (2004).

16. Bintanja, R., van de Wal, R. S. W. & Oerlemans, J. Modelled atmospheric temperatures and global sea levels over the past million years. *Nature* **437**, 125–128 (2005).

17. Mitrovica, J. X. & Milne, G. A. On post-glacial sea level: I. General theory. *Geophysical Journal International* **154**, 253–267 (2003).

18. Meehl, G. A. *et al.* Global climate projections. In *Climate Change 2007: The Physical Science Basis*, chap. 10, 747–845 (Cambridge University Press, Cambridge, UK, 2007).

19. Hastings, W. K. Monte Carlo sampling methods using Markov chains and their applications. *Biometrika* **57**, 97–109 (1970).

20. Hearty, P. J., Hollin, J. T., Neumann, A. C., O'Leary, M. J. & McCulloch, M. Global sea-level fluctuations during the Last Interglaciation (MIS 5e). *Quaternary Science Reviews* **26**, 2090–2112 (2007).

21. Schellmann, G. & Radtke, U. A revised morpho- and chronostratigraphy of the Late and Middle Pleistocene coral reef terraces on Southern Barbados (West Indies). *Earth-Science Reviews* **64**, 157–187 (2004).

22. Zhu, Z. R. *et al.* High-precision U-series dating of Last Interglacial events by mass spectrometry: Houtman Abrolhos Islands, western Australia. *Earth and Planetary Science Letters* **118**, 281–293 (1993).

23. Eisenhauer, A., Zhu, Z., Collins, L., Wyrwoll, K. & Eichstätter, R. The Last Interglacial sea level change: new evidence from the Abrolhos islands, West Australia. *International Journal of Earth Sciences* **85**, 606–614 (1996).

24. Westaway, R., Bridgland, D. & White, M. The Quaternary uplift history of central southern England: evidence from the terraces of the Solent River system and nearby raised beaches. *Quaternary Science Reviews* **25**, 2212–2250 (2006).

25. Clayton, K. Quantification of the impact of glacial erosion on the British Isles. *Transactions of the Institute of British Geographers* **21**, 124–140 (1996).

26. Braithwaite, C. J. R. Depositional history of the late Pleistocene limestones of the Kenya coast. *Journal of the Geological Society, London* **141**, 685–699 (1984).

27. Allen, J. R. L. Interglacial high-tide coasts in the Bristol Channel and Severn Estuary, southwest Britain: a comparison for the Ipswichian and Holocene. *Journal of Quaternary Science* **17**, 69–76 (2002).

28. Keen, D. H., Harmon, R. S. & Andrews, J. T. U series and amino acid dates from Jersey. *Nature* **289**, 162–164 (1981).

29. Bates, M. R., Keen, D. H. & Lautridou, J.-P. Pleistocene marine and periglacial deposits of the English Channel. *Journal of Quaternary Science* **18**, 319–337 (2003).

30. Giresse, P., Barusseau, J. P., Causse, C. & Diouf, B. Successions of sea-level changes during the Pleistocene in Mauritania and Senegal distinguished by sedimentary facies study and U/Th dating. *Marine Geology* **170**, 123–139 (2000).

31. Stea, R. R., Piper, D. J. W., Fader, G. B. J. & Boyd, R. Wisconsinan glacial and sea-level history of Maritime Canada and the adjacent continental shelf: A correlation of land and sea events. *GSA Bulletin* **110**, 821–845 (1998).

32. Stea, R., Fader, G., Scott, D. & Wu, P. Glaciation and relative sea-level change in Maritime Canada. In Weddle, T. K. & Retelle, M. J. (eds.) *Deglacial history and Relative Sea-Level Changes, Northern New England and Adjacent Canada*, no. 351 in Special Paper, 35–50 (Geological Society of America, Boulder, Colorado, 2001).

33. Cronin, T. M., Szabo, B. J., Ager, T. A., Hazel, J. E. & Owens, J. P. Quaternary climates and sea levels of the U.S. Atlantic Coastal Plain. *Science* **211**, 233–240 (1981).

34. Muhs, D. R., Simmons, K. R. & Steinke, B. Timing and warmth of the Last Interglacial period: new U-series evidence from Hawaii and Bermuda and a new fossil compilation for North America. *Quaternary Science Reviews* **21**, 1355–1383 (2002).

35. Chen, J. H., Curran, H. A., White, B. & Wasserburg, G. J. Precise chronology of the last interglacial period: ^{234}U-^{230}Th data from fossil coral reefs in the Bahamas. *Geological Society of America Bulletin* **103**, 82–97 (1991).

36. Tomazelli, L. J. & Dillenburg, S. R. Sedimentary facies and stratigraphy of a last interglacial coastal barrier in south Brazil. *Marine Geology* **244**, 33–45 (2007).

37. Rostami, K., Peltier, W. R. & Mangini, A. Quaternary marine terraces, sea-level changes and uplift

history of Patagonia, Argentina: comparisons with predictions of the ICE-4G (VM2) model of the global process of glacial isostatic adjustment. *Quaternary Science Reviews* **19**, 1495–1525 (2000).

38. Murray-Wallace, C. & Belperio, A. P. The Last Interglacial shoreline in Australia – a review. *Quaternary Science Reviews* **10**, 441–461 (1991).

39. Stirling, C. H., Esat, T. M., McCulloch, M. T. & Lambeck, K. High-precision U-series dating of corals from Western Australia and implications for the timing and duration of the Last Interglacial. *Earth and Planetary Science Letters* **135**, 115–130 (1995).

40. Stirling, C. H., Esat, T. M., Lambeck, K. & McCulloch, M. T. Timing and duration of the Last Interglacial: evidence for a restricted interval of widespread coral reef growth. *Earth and Planetary Science Letters* **160**, 745–762 (1998).

41. Hobday, D. K. Quaternary sedimentation and development of the lagoonal complex, Lake St. Lucia, Zululand. *Annals of the South African Museum* **71**, 93–113 (1975).

42. Ramsay, P. J. & Cooper, J. A. G. Late Quaternary sea-level change in South Africa. *Quaternary Research* **57**, 82–90 (2002).

43. Woodroffe, C. D. Late Quaternary sea-level highstands in the central and eastern Indian Ocean: A review. *Global and Planetary Change* **49**, 121–138 (2005).

44. Israelson, C. & Wohlfarth, B. Timing of the Last-Interglacial high sea level on the Seychelles Islands, Indian Ocean. *Quaternary Research* **51**, 306–316 (1999).

45. Braithwaite, C. J. R., Taylor, J. D. & Kennedy, W. J. The evolution of an atoll: The depositional and erosional history of Aldabra. *Philosophical Transactions of the Royal Society of London Series B* **266**, 307–340 (1973).

46. Brigham-Grette, J. & Hopkins, D. M. Emergent marine record and paleoclimate of the Last Interglaciation along the northwest Alaskan coast. *Quaternary Research* **43**, 159–173 (1995).

47. Gualtieri, L., Vartanyan, S., Brigham-Grette, J. & Anderson, P. M. Pleistocene raised marine deposits on Wrangel Island, northeast Siberia and implications for the presence of an East Siberian ice sheet. *Quaternary Research* **59**, 399–410 (2003).

48. Forman, S. L. & Miller, G. H. Time-dependent soil morphologies and pedogenic processes on raised beaches, Bröggerhalvöya, Spitsbergen, Svalbard Archipelago. *Arctic and Alpine Research* **16**, 381–394 (1984).

49. Andersson, T., Forman, S. J., Ingólfsson, Ó. & Manley, W. F. Late Quaternary environmental history of central Prins Karls Forland, western Svalbard. *Boreas* **28**, 292–307 (1999).

50. Landvik, J. Y., Lysa, A., Funder, S. & Kelly, M. The Eemian and Weicheselian stratigraphy of the Langelandslev area, Jameson Land, East Greenland. *Boreas* **23** (1994).

51. Vosgreau, H. *et al.* Paleoenvironments and changes in relative sea level during the last interglaciation at Langelandslev, Jameson Land, East Greenland. *Boreas* **23**, 398–411 (1994).

52. Gardner, N., Hall, B. & Wehmiller, J. Pre-Holocene raised beaches at Cape Ross, Southern Victoria Land, Antarctica. *Marine Geology* **229**, 273–284 (2006).

Supplementary Tables

Table S1: **Sites, Number, and Types of Sea Level Indicators in the LIG Database**

Site	# Observations	Type	Reference
Northeastern Atlantic Ocean and Mediterranean Sea			
Southern England	2	erosional	24
Bristol Channel, Britain	1	erosional	27
Belle Hogue Cave, Jersey	1	erosinal	28
Port-Racine Beach, France	1	erosional	29
The Netherlands	8	facies	7
Hergla South, Tunisia	2	facies	20
Quaternary Basin, Mauretania	2	facies	30
Northwestern Atlantic Ocean and Carribean Sea			
Cape George, Nova Scotia	1	erosional	31,32
Mark Clark, South Carolina	1	facies	33
Grape Bay, Bermuda	2	facies	20,34
San Salvador Island, Bahamas	3	reef	35
Great Inagua Island, Bahamas	3	reef; erosional	35
Abaco Island, Bahamas	3	reef; erosional	20
Southern Barbados	8	reef	21
Southwestern Atlantic Ocean			
Rio Grande do Sol coastal plain, Brazil	1	facies	36
Camarones, Patagonia, Argentina	1	erosional	37
Pacific Ocean			
Oahu, Hawaii	3	reef; corals; facies	20,34
Mururoa Atoll	1	corals	2
Australia			
Eyre Peninsula	1	facies	38
Rottnest Island	1	reef	20,39
Minim Cove	1	facies	20
Cape Range	2	reef	40

Continued on Next Page. . .

Table S1: **Sites, Number, and Types of Sea Level Indicators in the LIG Database**

Site	# Observations	Type	Reference
Houtman Abrohlos Islands	8†	reef; facies; corals	22,23
Indian Ocean and Red Sea			
Red Sea	30	isotopic	6
KwaZulu-Natal, South Africa	3	erosional; facies	41,42
Eastern Cape, South Africa	1	erosional	42
Maldives Archipelago	1	facies	43
La Digue Island, Seychelles	2	reef	44
Aldabra Atoll, Seychelles	3	corals; facies	45
Polar regions			
Northern and Western Alaska	3	facies	46
Wrangel Island, Siberia	1	facies	47
Western Spitsbergen	3	erosional	48,49
Scoresby Sund, Greenland	3	facies	50,51
Cape Ross, Antarctica	1	erosional	52

† Three observations removed due to mismatch with age model.

Table S2: Summary statistics for different Gaussian taper widths and data subsets.

Taper (ky)	Subset	Max. Median GSL Age (ky)	Level (m)	GSL exceed. levels (m) 95%	67%	33%	Rate exceed. levels (m/ky) 95%	67%	33%
3	Std.	124	7.0 ± 1.4	6.6	8.0	9.4	5.6	7.4	9.2
2	Std.	124	6.9 ± 1.3	6.3	7.6	8.7	5.7	7.5	9.1
4	Std.	124	7.3 ± 1.3	6.5	7.8	8.9	5.7	7.5	9.1
-	Std.	131	13.0 ± 15.2	6.7	8.5	12.6	6.0	8.1	10.9
3	Full	124	7.0 ± 1.4	6.6	8.1	10.1	5.8	8.0	10.7
3	-Cor.	123	7.2 ± 1.8	5.8	7.5	8.9	5.8	7.9	9.6
3	-Eros.	124	6.8 ± 1.3	5.9	7.2	8.4	5.3	7.3	9.1
3	-Fac.	124	7.7 ± 1.4	6.3	7.7	8.8	5.5	7.3	8.9
3	-Iso.	127	6.8 ± 3.2	7.0	8.7	10.5	3.9	6.5	9.5
3	+Cor.	128	8.7 ± 2.0	6.2	8.3	10.0	-0.1	4.0	8.0
3	+Ero.	128	6.4 ± 7.2	-0.3	3.9	6.8	-8.0	1.4	6.3
3	+Fac.	119	6.7 ± 2.5	6.1	8.0	9.7	1.2	4.7	7.3
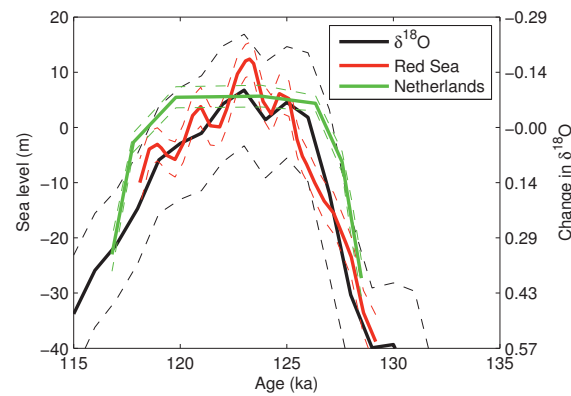
Figure S1: The oxygen isotope-based estimate of global sea level (black) and local sea level curves from the Red Sea (red) and the Netherlands (green). Dashed lines show 1σ confidence intervals in sea level. The initial best alignment of the three curves is shown. On the right axis, the black curve also shows the deviation of the underlying global oxygen isotope stack from its present-day value of $3.23 \pm 0.03\text{‰}$ (PDB)[3].
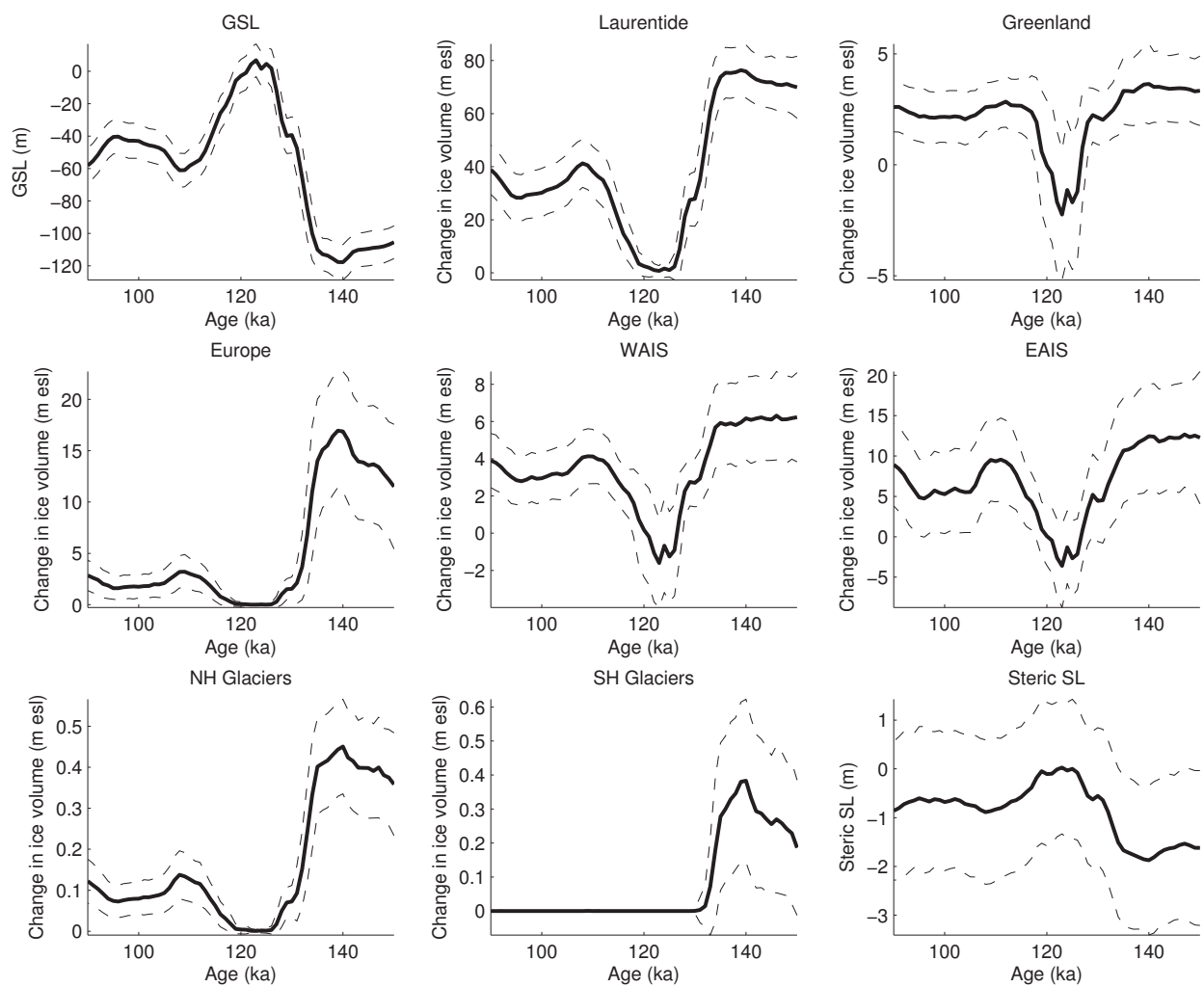
Figure S2: Distributions of global sea level, changes in ice sheet volumes, and steric sea level in the 250 alternative histories used to construct the prior distribution. Dashed lines show 1σ ranges.
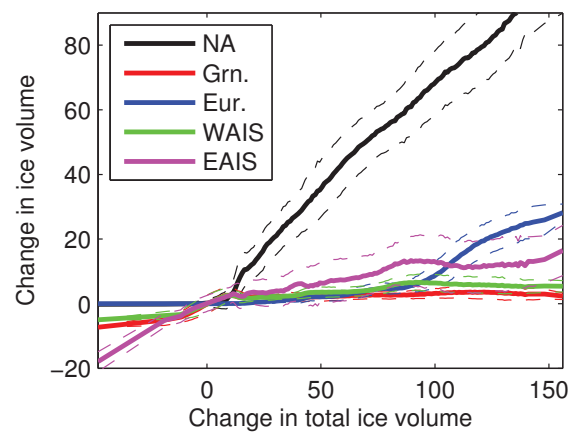
Figure S3: Mean and standard deviation of the change in volume of each ice sheet as a function of change in total ice volume. Dashed lines show 1σ ranges.
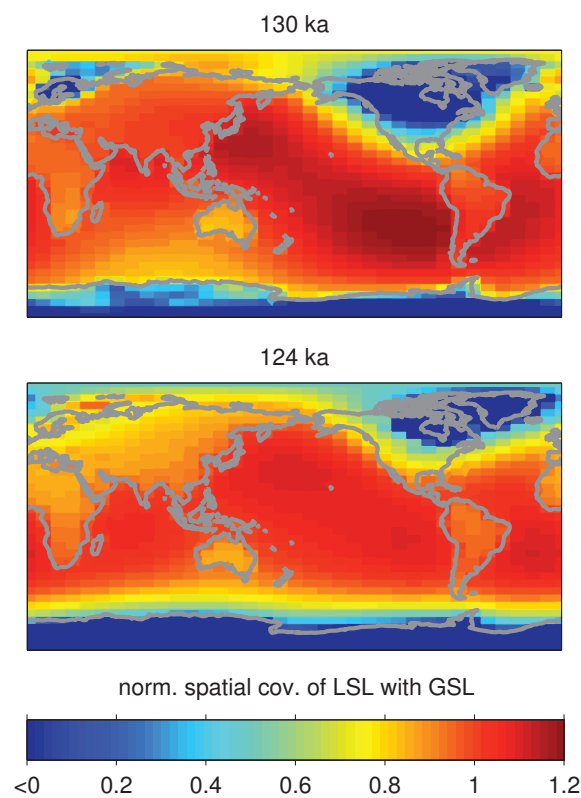
Figure S4: The spatial covariance of local sea level with global sea level at 130 ka and 124 ka, normalized to the contemporaneous variance of global sea level (σ_{GSL} = 11.6 m at 130 ka and 10.5 m at 124 ka).
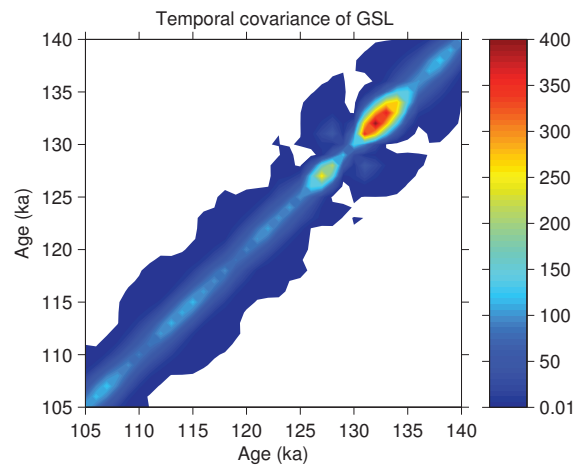
Figure S5: The covariance of GSL over time as employed in the main analysis (with a 3 ky Gaussian taper).

In the unshaded areas, the covariance is less than 0.01.
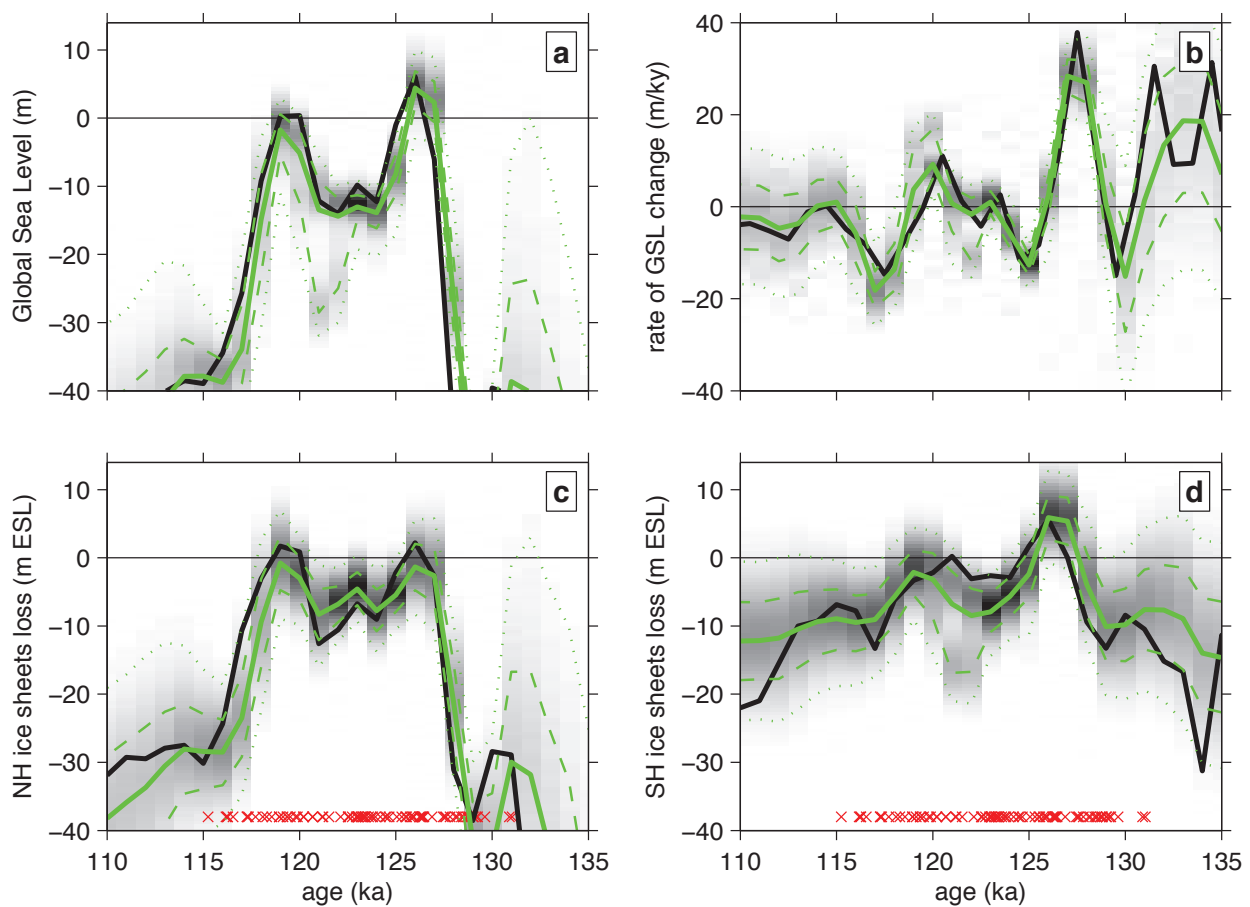
Figure S6: Reconstructed (a) GSL, (b) GSL rate, (c) NH ice volume and (d) SH ice volume for a synthetic sea level history. The heavy green lines mark the median projections based on the statistical analysis of pseudo-proxies, while the dashed lines mark the 16th and 84th percentiles, and dotted lines mark the 2.5th and 97.5th percentiles. The heavy black lines mark the "true" values.
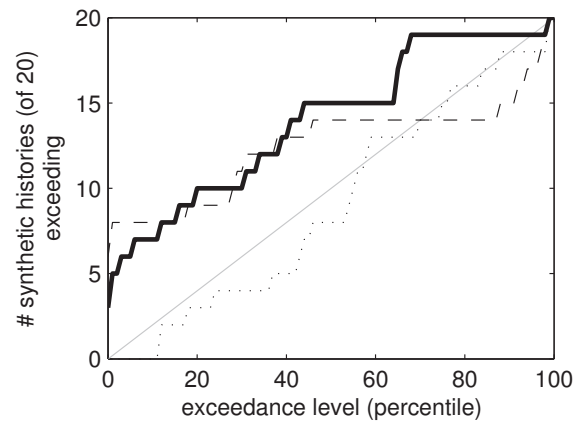
Figure S7: Number of synthetic histories (out of 20) in which the "true" maximum value exceed a given exceedance value. The heavy solid line shows global sea level rise, the dashed line shows the 1000-year average rate of change of global sea level when global sea level is at or above -10 m, and the dotted line shows ice loss in the hemisphere with the least ice loss. The grey line indicates the expected values if the distribution of synthetic histories conformed precisely to the distribution specified by the exceedance values.
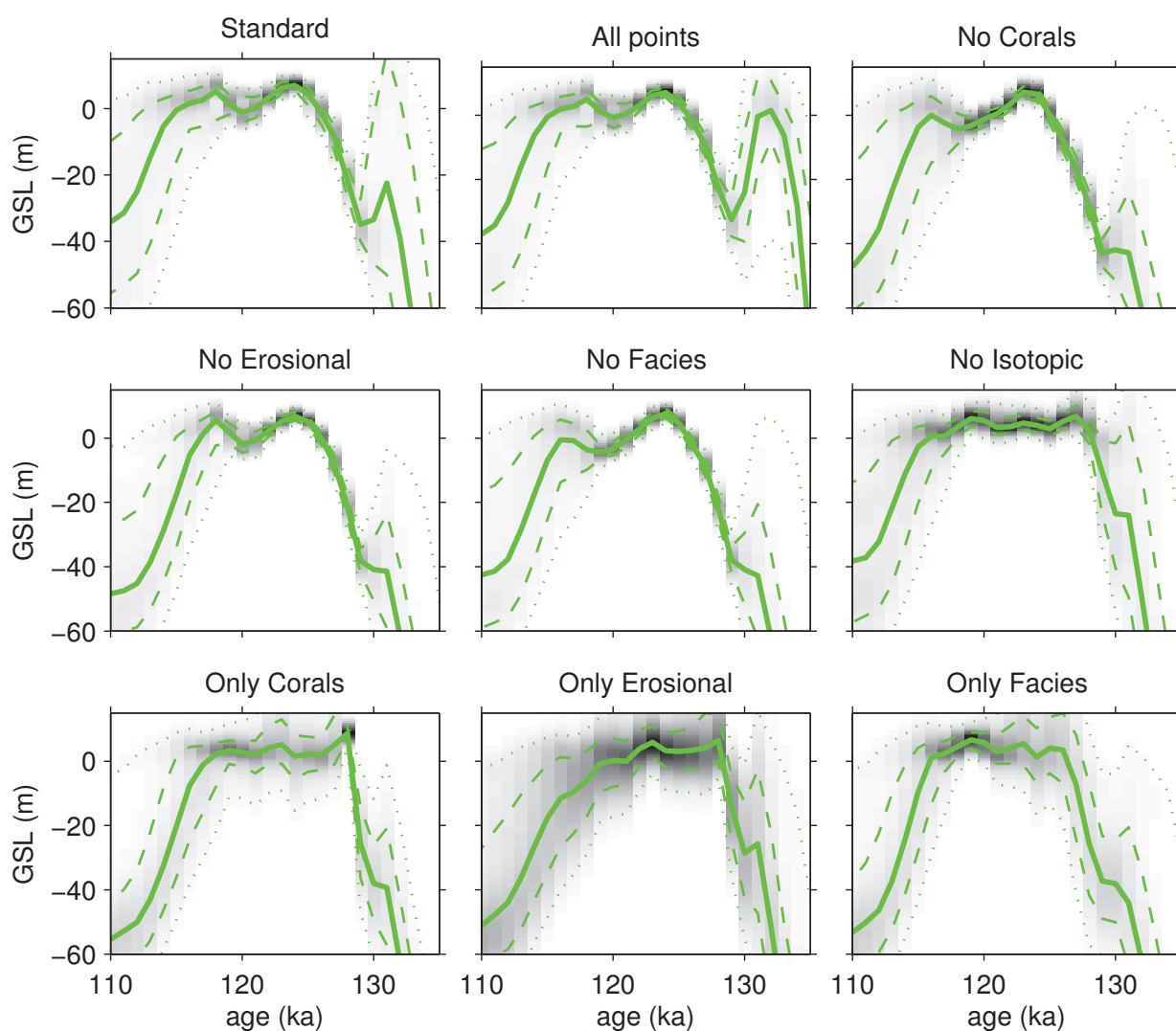
Figure S8: Projections of GSL using different subsets of the data. The "standard" subset excludes three data points from the Houtman Abrohlos islands that are inconsistent with the age model, while the "full subset" includes them. The remaining seven subsets either exclude or consist only of measurements based on corals, erosional features, facies interpretations, or the Red Sea isotope curve. The heavy lines mark the median projections, dashed lines mark the 16th and 84th percentiles, and dotted lines mark the 2.5th and 97.5th percentiles. Summary statistics are provided in Table S2.
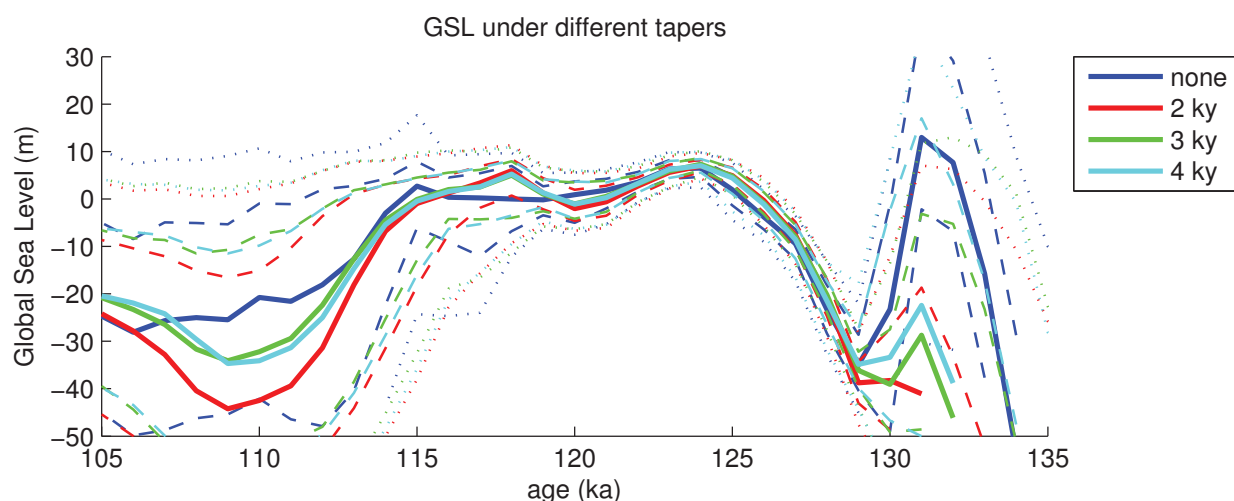
Figure S9: GSL projections using different width Gaussian temporal taper functions in the covariance function. Summary statistics are provided in Table S2. The heavy lines mark the median projections, dashed lines mark the 16th and 84th percentiles, and dotted lines mark the 2.5th and 97.5th percentiles.]
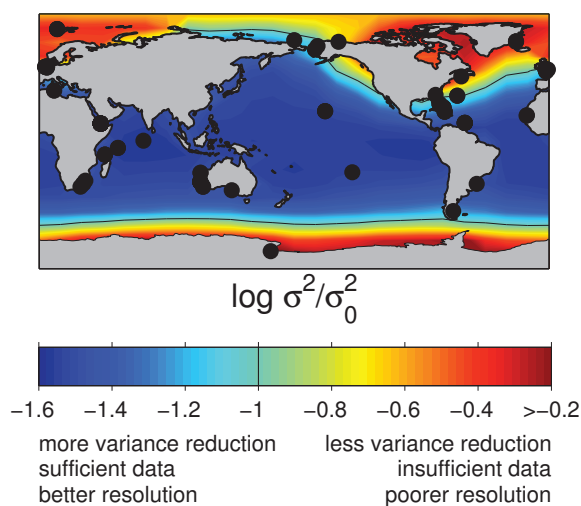

Figure S10: Map of the data need index. We calculate this index by averaging the ratio of the posterior variance to the prior variance over the time period between 114 and 129 ka.

GLOBAL CHANGE

Interglacial and future sea level

Peter U. Clark and Peter Huybers

A merger of data and modelling using a probabilistic approach indicates that sea level was much higher during the last interglacial than it is now, providing telling clues about future ice-sheet responses to warming.

Predicting sea-level rise in a warming world is one of science's great challenges. According to sea-rise projections for the twenty-first century, the 145 million people living within a metre of the present sea level risk losing their land and their homes. Many more would be affected by the resulting socio-economic disruption[1]. Our poor understanding of ice-sheet dynamics means that projecting sea-level rise beyond the twenty-first century is much less certain[2]. On page 863 of this issue, however, Kopp *et al.*[3] derive a new assessment of sea level during the last interglacial, around 125,000 years ago, that provides insight into this question. If their results are correct, the sea-level rise over the coming century will be followed by many more metres of rise over the ensuing centuries.

Increases in global sea level stem from both expansion of warming water (thermosteric change) and addition of new water from melting ice on land (eustatic change). Predictions of future thermosteric changes are relatively well constrained compared with those of the eustatic change associated with melting of the Greenland and Antarctic ice sheets[4]. There is thus a need to better determine both how much and how rapidly eustatic sea level will rise in response to a given forcing effect such as anthropogenic global warming.

Evidence that sea level during the last interglacial was 4–6 metres higher than at present has long been proposed as a possible analogue for the equilibrium sea-level response to future anthropogenic warming[5,6]. But the sea-level records may include a local response to geophysical adjustments from the preceding glaciation, and thus may not accurately record the global sea level[7]. Furthermore, the implications of 4 or 6 m of rise are quite different: if sea level increases by only 4 m, much of it can be reconciled as being due to thermosteric rise and partial loss of the Greenland ice sheet; anything more requires a contribution from Antarctica.

Kopp *et al.*[3] reach the startling conclusion that, during the last interglacial, global sea level was at least 6.6 m above present, and may have reached 9.4 m, much higher than previous estimates. The implication is that both the Greenland and Antarctic ice sheets were much smaller 125,000 years ago.

To derive this result, Kopp *et al.* compiled a database of proxy measurements of sea level that includes isotopic and coral records, as well as other records that are less well dated. Although this database is more comprehensive than those used in previous studies, constraining estimates for past global sea level from noisy and sparse data whose timing is uncertain is a formidable statistical problem. It is particularly difficult because one must also account for regionally varying geophysical effects, including local tectonic uplift or subsidence, and sea-level changes induced by gravitational, deformational and rotational effects associated with the redistribution of ice, ocean and mass of the solid Earth[8]. Using a physical model that includes these effects, Kopp *et al.* derived an estimate of the covariance between local and global sea level. They then merged the local–global covariance estimate with proxy estimates of sea level within a Bayesian framework to make temporally complete estimates of global sea level and assess their probability.

The redistribution of mass associated with individual ice-sheet melting causes distinct

Figure 1 | Similarity of latitudinal warming (ΔT) during the last interglacial and a projection for the late twenty-first century. The green line summarizes proxy-data estimates of sea surface and air temperature during the last interglacial relative to the present interglacial before industrialization. Diamonds are largely sea surface temperatures, but include temperatures derived from polar ice cores and two high-latitude Northern Hemisphere pollen records. The temperatures reflect the interval between 120,000 and 130,000 years ago (mean and 1 standard deviation). The green line is a polynomial fit to these data. Surface air temperature estimates from less-well-dated pollen sites in Europe (not shown) similarly show warmer temperatures across most of Europe during the last interglacial[17]. The blue solid line is the zonal mean of the projected surface temperature changes (with 1 standard deviation shown by dotted blue lines) for the late twenty-first century relative to 1980–99; it is based on the SRES B1 greenhouse-gas-emission scenario obtained using the GFDL climate model. (Palaeoclimate data are available at www.ncdc.noaa.gov/paleo/pubs/clark2009.)

spatial patterns in sea level[9]. In conjunction with the proxy measurements, Kopp *et al.*[3] also used the modelled patterns to estimate that Greenland and Antarctica each contributed at least 2.5 m of sea-level rise. This estimate is consistent with independent constraints: the maximum Greenland contribution was probably 3.4 m (ref. 10), and the thermosteric plus mountain-glacier and ice-cap contribution was probably no more than 1 m. So, if sea level was at least 6.6 m higher, a minimum of 2.2 m must have come from Antarctica. The Antarctic contribution would probably have come from the inherently unstable West Antarctic Ice Sheet, which locks up the equivalent of at least 3.3 m of sea level[11], so that Kopp and colleagues' result implies that most, if not all, of this ice sheet melted about 125,000 years ago.

Perhaps of greatest socio-economic concern is the possible maximum rate of sea-level rise in a warmer world. According to Kopp *et al.*[3], sea-level rise during the last interglacial was in the range of 6–9 millimetres per year. By comparison, instrumental records indicate that the rate of global sea-level rise over the twentieth century was about 2 mm yr^{-1}. That may have accelerated between 1993 to 2003 to around 3 mm yr^{-1}, at least in part due to an acceleration in mass loss from the Greenland and Antarctic ice sheets[12].

Why was sea level so much higher 125,000 years ago? One possibility is that ice sheets have multiple potential steady states for a given climate[13]. However, the global temperature was apparently 1.5–2 °C warmer than the pre-anthropogenic global average of the past 10,000 years (Fig. 1), despite there being essentially no difference in atmospheric greenhouse-gas concentrations. Climate models have simulated a strong Northern Hemisphere summer warming in response to Earth's more eccentric orbit during the last interglacial, but almost no change in the Southern Hemisphere[14]. Southern warming may then have occurred through an oceanic teleconnection with the north[15], or through changes in the duration of the Southern Hemisphere summer[16], with accompanying feedbacks amplifying this warming.

In any event, the latitudinal distribution of warming seems to be remarkably similar to the global temperature response to carbon dioxide under a commonly used scenario for greenhouse-gas emissions (compare the green and blue lines in Fig. 1). This suggests that the climate of the last interglacial might, by coincidence, provide a reasonable analogue for establishing ice-sheet sensitivity to global warming. Assuming that Kopp and colleagues' estimates are accurate, and that higher sea level resulted from higher temperatures, the disconcerting message is that the
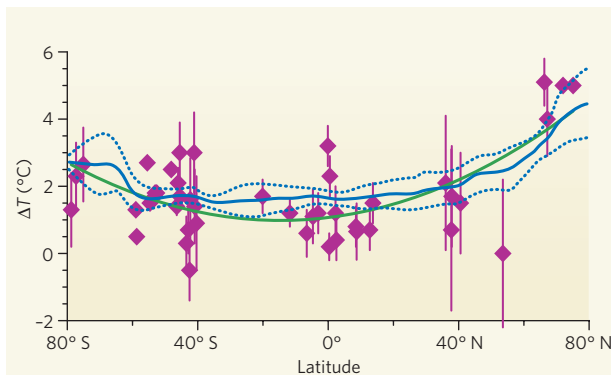
equilibrium response of sea level to 1.5–2 °C of global warming could be an increase of 7–9 metres. ■

Peter U. Clark is in the Department of Geosciences, Oregon State University, Corvallis, Oregon 97331, USA. Peter Huybers is in the Department of Earth and Planetary Sciences, Harvard University, Cambridge, Massachusetts 02138, USA.
e-mails: clarkp@onid.orst.edu; phuybers@fas.harvard.edu

1. Anthoff, D., Nicholls, R. J., Tol, R. S. J. & Vafeidis, A. *Tyndall Centre Working Pap.* 96 (2006).
2. Alley, R. B., Clark, P. U., Huybrechts, P. & Joughin, I. *Science* 310, 456–460 (2005).
3. Kopp, R. E., Simons, F. J., Mitrovica, J. X., Maloof, A. C. & Oppenheimer, M. *Nature* 462, 863–867 (2009).
4. Meehl, G. A. *et al.* in *Climate Change 2007: The Physical Science Basis* (eds Solomon, S. D. *et al.*) 747–845 (Cambridge Univ. Press, 2007).
5. Mercer, J. H. *Nature* 271, 321–325 (1978).
6. Jansen, E. *et al.* in *Climate Change 2007: The Physical Science Basis* (eds Solomon, S. D. *et al.*) 433–497 (Cambridge Univ. Press, 2007).
7. Lambeck, K. & Nakada, M. *Nature* 357, 125–128 (1992).
8. Mitrovica, J. X. & Milne, G. A. *Geophys. J. Int.* 154, 253–267 (2003).
9. Mitrovica, J. X., Tamisiea, M. E., Davis, J. L. & Milne, G. A. *Nature* 409, 1026–1029 (2001).
10. Otto-Bliesner, B. L. *et al. Science* 311, 1751–1753 (2006).
11. Bamber, J. L., Riva, R. E. M., Vermeersen, B. L. A. & LeBrocq, A. M. *Science* 324, 901–903 (2009).
12. Velicogna, I. *Geophys. Res. Lett.* doi:10.1029/2009GL040222 (2009).
13. Pollard, D. & DeConto, R. M. *Global Planet. Change* 45, 9–21 (2005).
14. Crowley, T. J. & Kim, K.-Y. *Science* 265, 1566–1568 (1994).
15. Duplessy, J. C., Roche, D. M. & Kageyama, M. *Science* 316, 89–91 (2007).
16. Huybers, P. & Denton, G. *Nature Geosci.* 1, 787–792 (2008).
17. Kaspar, F., Kühl, N., Cubasch, U. & Litt, T. *Geophys. Res. Lett.* doi:10.1029/2005GL022456 (2005).

DNA REPAIR

A heavyweight joins the fray

Simon J. Boulton

Tagging of DNA-damage-associated proteins by ubiquitin is key to coordinating the DNA-damage response. The ubiquitin-related protein SUMO is revealed as a crucial regulator of ubiquitylation in DNA repair.

Ubiquitylation — the attachment of ubiquitin groups to cellular proteins — was initially characterized by its role in promoting protein destruction. However, we now know that the consequences of ubiquitylation are diverse, and that it affects many cellular systems. The ubiquitin modification comes in many flavours (addition of a single ubiquitin molecule, for example, or of polyubiquitin chains that differ in the position of the linkage between ubiquitin molecules), and the various types of ubiquitylation can alter the fate of target proteins in different ways. In addition, the cell has ubiquitin-related modifiers, such as the SUMO proteins, that also alter protein fate or function after conjugation[1]. One process that has been inextricably linked to ubiquitylation is the cellular response to DNA damage. Although studies[2,3] had suggested a link between the DNA-damage response and the SUMO pathway, proof that SUMOylation is important for DNA repair had remained elusive. In this issue, two groups, Morris *et al.*[4] (page 886) and Galanty *et al.*[5] (page 935), now provide good evidence that SUMO functions together with ubiquitin to coordinate DNA repair.

DNA double-strand breaks (DSBs) result in the recruitment and activation of the protein kinases ATM, ATR and DNA-PK, which phosphorylate target proteins, such as the variant histone H2AX. The phosphorylated proteins then promote the recruitment of other DNA-repair proteins to DSBs[6], including MDC1 (mediator of the DNA-damage checkpoint), 53BP1 and the E3 ubiquitin ligases RNF8, RNF168 and BRCA1 (ref. 6), which catalyse ubiquitylation events[7] at DSBs. (Conjugation of ubiquitin or related modifiers to target proteins requires an E1 activating enzyme, an E2 conjugating enzyme and an E3 ligase.)

To investigate the involvement of the SUMO pathway in the DNA-damage response, Morris *et al.*[4] and Galanty *et al.*[5] analysed the subcellular localization of SUMO-pathway components in mammalian cells. Both groups[4,5] report that the E1 SUMO-activating enzyme SAE1, the E2 SUMO-conjugating enzyme UBC9, and the three forms of vertebrate SUMO protein, SUMO1 and the closely related SUMO2 and SUMO3 (SUMO2/3), are recruited to DSBs.

The authors[4,5] used RNA interference and fluorescence microscopy to show that the SUMO E3 ligases PIAS1 and PIAS4 are responsible for SUMOylation events at DSBs. Depletion of PIAS1 impaired accumulation of SUMO2 and SUMO3 (but not SUMO1) at DSBs, whereas depletion of PIAS4 impaired recruitment of SUMO1 and SUMO2/3. Furthermore, recruitment of 53BP1 to DSBs depended on PIAS4, whereas recruitment of BRCA1 depended on both PIAS1 and PIAS4. Is SUMOylation necessary for DSB repair? The answer is, emphatically, yes — cells lacking PIAS1 or PIAS4 showed defects in DSB repair and were also highly sensitive to DSBs caused by ionizing radiation.

What are the targets of the SUMO pathway during the DNA-damage response? Prompted by a study showing interaction between UBC9 and BRCA1 in the nematode worm *Caenorhabditis elegans*[2], both groups[4,5] independently showed that BRCA1 is SUMOylated during the DNA-damage response in a PIAS1- and PIAS4-dependent manner (Fig. 1). Depletion of PIAS1 and PIAS4 impaired recruitment of BRCA1 to DSBs[4,5], significantly impaired ubiquitylation at DSBs, and reduced ubiquitylation of the histones H2A and H2AX; the latter process has been shown to require
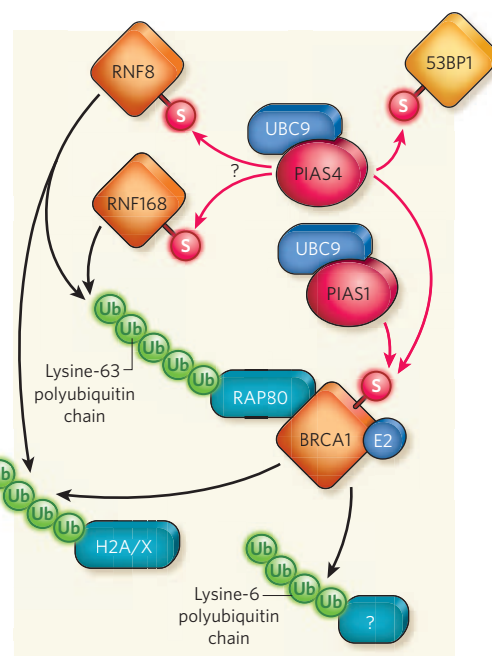

Figure 1 | Ubiquitylation and SUMOylation at DSBs. Double-strand DNA breaks (DSBs) result in the recruitment of DNA-repair proteins, including 53BP1 and the E3 ubiquitin ligases RNF8, RNF168 and BRCA1. Morris *et al.*[4] and Galanty *et al.*[5] observe that the SUMO-pathway components UBC9–PIAS4 and UBC9–PIAS1 also accumulate at DSBs, where they catalyse the SUMOylation of 53BP1 and BRCA1 (and possibly RNF8 and RNF168). SUMOylation stimulates BRCA1 E3 ubiquitin-ligase activity, leading to ubiquitylation of target proteins at DSBs, including the histone H2A and its variant H2AX. H2A and H2AX are also substrates for ubiquitylation by RNF8 and RNF168, as is RAP80, a ubiquitin-binding protein that also interacts with BRCA1. RNF8 and RNF168 catalyse the formation of lysine-63-linked ubiquitin chains, whereas BRCA1 and its E2 conjugating enzyme catalyse the formation of lysine-6-linked ubiquitin chains. S, SUMO; Ub, ubiquitin. Red arrows indicate SUMOylation; black arrows indicate ubiquitylation.

the ligase activities of RNF8, RNF168 and BRCA1 (ref. 7). Galanty *et al.*[5] also showed that 53BP1 is SUMOylated and that this affects its retention at DSBs.

RNF8 and RNF168 catalyse the formation